PspA maintains membrane integrity by an ESCRT-like membrane remodeling activity

Benedikt Junglas[1,2,4], Stefan T. Huber[3], Thomas Heidler[1,2], Daniel Mann[1,2], Raoul Hennig[4], Mairi Clarke[3], Julio O. Ortiz[1,2], Dirk Schneider[4*], and Carsten Sachse[1,2,3,5*]

[1]Ernst-Ruska Centre for Microscopy and Spectroscopy with Electrons (ER-C-3/Structural Biology), Forschungszentrum Jülich, 52425 Jülich, Germany.

[2]JuStruct: Jülich Center for Structural Biology, Forschungszentrum Jülich, 52425 Jülich, Germany

[3]European Molecular Biology Laboratory (EMBL), Structural and Computational Biology Unit, Meyerhofstraße 1, 69117 Heidelberg, Germany

[4]Institute of Chemistry, Biochemistry, Johannes Gutenberg University Mainz, 55128 Mainz, Germany.

[5]Department of Biology, Heinrich Heine University, Universitätsstr.1, 40225 Düsseldorf, Germany

* Correspondence should be addressed to: dirk.schneider@uni-mainz.de, c.sachse@fz-juelich.de

Keywords: PspA, IM30, Vipp1, ESCRT-III, helical reconstruction, cryo-EM, membrane remodeling

Summary

The phage shock proteins (Psp) system is activated in bacteria in response to various membrane stress conditions. PspA, the main Psp effector, preserves the integrity and functions of the bacterial inner membrane. Here, we present the 3.6 Å resolution cryo-EM structure of PspA assembled in helical rods. The structure reveals that PspA adopts a canonical ESCRT-III fold in an extended open conformation with the C-terminal helix facing the outside of the helical tube. In addition to the structural homology, we visualized how PspA fuses small vesicles into µm-sized vesicles when reconstituted with bacterial membrane lipids. This membrane remodeling activity is in line with the functional properties of ESCRT-III family proteins. Our structural and functional analyses reveal that bacterial PspA belongs to the evolutionary ancestry of ESCRT-III proteins involved in membrane remodeling.

Introduction

Membrane remodeling and re-shaping is crucial for cell viability in all domains of life. In order to maintain the integrity of internal membranes under stress conditions, many bacteria activate the phage shock protein (Psp) system. A key component of this multi-protein system is the effector protein PspA that interacts with other Psp members and membrane lipids to stabilize bacterial membranes (Joly et al., 2010). For the currently best studied *E. coli* Psp system, it has been shown that cytoplasmic PspA binds and thereby inactivates the transcription factor PspF under non-stress conditions (Joly et al., 2010). After stress stimulation, signaling activates the Psp response system by the release of PspF from PspA. Free PspA can bind peripherally to the cytoplasmic face of bacterial inner membranes via interaction with negatively charged membrane lipids (Jovanovic et al., 2014) and thereby counteracts membrane stress (Joly et al., 2010; Manganelli and Gennaro, 2017). This way, membrane-bound PspA has, for instance, been shown to block proton leakage of isolated damaged membranes (Kobayashi et al., 2007). More recently, a membrane protecting protein carpet mechanism has been proposed for the PspA-homologous cyanobacterial protein IM30 (inner membrane associated protein of 30 kDa, alternatively known as Vipp1) (Junglas et al., 2020). Moreover, upon homologous overexpression of the *E. coli* PspA (*Eco*PspA), higher-order structures were observed, which originated from membrane-associated fractions (Standar et al., 2008). In support, members of the PspA family may also function in membrane surveillance and repair via tethering and sealing stress-induced membrane lesions, presumably by triggering lipid bilayer fusion (Siebenaller et al., 2020). Indeed, membrane fusion activity has been reported previously for the PspA homolog IM30 of the cyanobacterium *Synechocystis* sp. PCC 6803 (Hennig et al., 2015).

While the Psp response system appears to be conserved in Gram-negative bacteria, Psp's have also been identified in cyanobacteria, archaea as well as in chloroplasts (Manganelli and Gennaro, 2017). Yet, solely homologs of PspA, the key effector protein of the Psp response system, appear to be strictly conserved and thus critical for membrane protection and remodeling (Manganelli and Gennaro, 2017). The homologous proteins PspA, IM30 and LiaH are part of a bacterial membrane remodeling family that shares many structural and functional features for maintaining membrane integrity (Thurotte et al., 2017). Previously,

*Eco*PspA was found to form large, homo-oligomeric rings in solution with outer diameters of ~20 nm and a molecular mass of about 1 MDa (Hankamer et al., 2004), as well as higher-order rod structures (Male et al., 2014). Similarly, the PspA homologous proteins LiaH and IM30 form rings (Aseeva et al., 2004; Fuhrmann et al., 2009; Saur et al., 2017; Wolf et al., 2010), while IM30 also forms rod structures (Fuhrmann et al., 2009; Theis et al., 2019, 2020; Vothknecht et al., 2012). In addition to the shared property to form large homo-oligomeric structures, the predicted secondary structure and some sequence motifs of PspA/LiaH/IM30 are conserved (Bultema et al., 2010; Thurotte et al., 2017; Vothknecht et al., 2012). The three proteins share six predicted helices, whereas IM30 contains an additional seventh C-terminal α-helix connected by a flexible linker (Bultema et al., 2010). The structure of an extended α-helical hairpin formed by the 2nd and 3rd *Eco*PspA helices was resolved by X-ray crystallography (Osadnik et al., 2015), yet the full-length PspA structure is not known to date.

Although most membrane-remodeling proteins such as epsin, dynamin or BAR domain-containing proteins were first characterized in eukaryotes (Ford et al., 2002; Frost et al., 2009; Praefcke and McMahon, 2004), membrane remodeling is a common process in all three domains of life. Several bacterial proteins, such as a dynamin-like protein and the bacterial tubulin-homologue FtsZ (Low et al., 2009; Szwedziak et al., 2014), have been demonstrated to be involved in membrane remodeling (Bohuszewicz et al., 2016). In some archaea, the gene products of the cell division machinery CdvB/CdvC were identified as homologues of the well-characterized eukaryotic protein family of endosomal sorting complexes required for transport (ESCRT) (Lindås et al., 2008; Samson et al., 2008). They were originally characterized in eukaryotic membrane trafficking events of multivesicular body biogenesis (Katzmann et al., 2001), viral budding (Garrus et al., 2001) and cytokinesis (Carlton and Martin-Serrano, 2007).

ESCRT proteins have been shown to be involved in a series of very diverse membrane remodeling processes in eukaryotic cells, which include nuclear envelope sealing (Vietri et al., 2015), plasma membrane repair, lysosomal protein degradation (Zhu et al., 2017) and closure of autophagosomes (Takahashi et al., 2018; Zhen et al., 2020). Despite this functional diversity, the responsible core proteins belong to a single

conserved group of ESCRT-III proteins. Depending on the species, different ESCRT-III isoforms exist, and 8 or 12 isoforms are known in yeast and humans, respectively. ESCRT-III proteins comprise approx. 220 amino acids and share seven predicted α-helices. Initial X-ray crystallographic studies of truncated CHMP3 revealed a compact structure made of a four-helix bundle comprising of a long α-helical hairpin motif (Muzioł et al., 2006). More recently, polymers assembled from full-length ESCRT-III were elucidated at near-atomic resolution using cryo-EM: human IST1 and CHMP1B make up a hetero-polymer with a compact and extended conformation forming a tubular assembly (McCullough et al., 2015), whereas yeast Vps24 assembles in a double-stranded filament composed of domain-swapped dimers in the extended conformation (Huber et al., 2020). Although these two structures have the predicted α-helical stretches in common, how the helices combine to a tertiary structure differs between these two structures. It has been shown that mixing of different ESCRT proteins in a particular order is required to assemble hetero-polymeric complexes that drive membrane remodeling *in vitro* (Caillat et al., 2019; Huber et al., 2020; Pfitzner et al., 2020). Downstream of the ESCRT-III activity is the AAA-ATPase Vps4 that promotes assembly and disassembly of ESCRT-III complexes and thereby contributes to membrane remodeling.

Despite the known critical roles of ESCRT-III proteins in the Archaea and Eukarya kingdom, members of a conserved bacterial ESCRT family have not yet been identified, neither by sequence analysis or structural comparison nor by functional characterization. In the current study, we determined the 3.6 Å resolution cryo-EM structure of PspA assembled in helical tubes. The built atomic model reveals that PspA adopts a canonical ESCRT-III fold, making up the wall of the tubular assemblies. When PspA rods are reconstituted with small lipid vesicles, they modulate the lipid bilayer structure via membrane interaction and induce vesicle fusion. The cryo-EM structure combined with biochemical lipid remodeling experiments show that bacterial PspA is a *bona fide* member of an evolutionary conserved ESCRT-III family.

Results

PspA rods are tubular assemblies with helical symmetry

In order to structurally investigate the membrane protective mechanism of PspA, we overexpressed and purified PspA of the cyanobacterium *Synechocystis* sp. PCC 6803. Subsequently, we visualized the PspA preparations using cryo-EM. The acquired micrographs show elongated rod assemblies with around 20 nm in width and varying lengths of up to several hundreds of nanometers (**Figure 1A**). We characterized the rods by 2D classification using a large data set of 8,342 micrographs and found that approx. 40 % of the segmented rods had a consistent diameter of 20 ± 1 nm, whereas the remaining rods showed larger diameters (**Figure S1**). Closer analysis of the most homogeneous segments revealed a basic Christmas-tree pattern with a longitudinal repeat every 30 Å indicative of a repeating pitch and a detailed pattern of features typical for helical assemblies in the center of the 2D class average (**Figure 1B**). The corresponding power spectrum showed a layer line pattern diffracting to approx. 7 Å resolution (**Figure 1C**). Based on this class average and a smaller cleaned-up subset, we worked out that the majority of PspA rods is organized in a helical assembly with a helical rise and rotation of 2.9 Å and 35.3º per subunit. Using a total of 139,300 asymmetric units, we then determined the cryo-EM structure at an overall resolution of 3.6 Å (**Figure 1D**), with the best resolution of 3.5 Å at 50 Å radial distance and decreasing to 4.7 Å resolution at 100 Å radial distance from the center of the helical tube (**Figure 1E**). After density segmentation, we found that a single subunit has an elongated shape of 180 x 20 Å dimension, which is positioned perpendicular to the rod axis (**Figure 1F**). When seen in top view, the subunit extends over one third of the rod's cross section. In side view, the subunits are arranged like overlapping bricks that constitute the wall of the helical rod (**Figure 1G**).

PspA adopts an elongated four-helix core with an accessory C-terminal helix

Using the segmented density, we built an atomic model of a PspA monomer, covering residues 22 to 217 arranged in five α helices connected by loops (**Figure 2A-C**). At one end of the elongated subunit, we identified a density that corresponds to the determined structure of a long α-helical hairpin PspA fragment (PDB-ID 4WHE, (Osadnik et al., 2015)) and that independently confirmed the chosen handedness of the

cryo-EM map (**Figure 2D**). The observed density at the hairpin matches the features expected at the estimated resolution. The best resolved density stretch accommodates helices α1-α4 (25-185), *e.g.* helix α1 (**Figure 2E**) and helix α2+3 (**Figure 2F**), making up the elongated four-helix core thereby constituting the wall of the tubular assembly. Unfortunately, we did not find density corresponding to a predicted N-terminal helix α0 (4-21) (**Figure S2A**) in the inner lumen of the rod. Attached to the outer wall of the helical rod, however, we identified density accommodating the amphipathic helix α5 (191-215) (**Figure 2G, Figure S2B**) that is positioned longitudinally with respect to the rod axis in contrast to the long transverse direction of the subunit core. Moreover, the density of helix α5 displays a poorer local resolution of 4.7 Å, and the corresponding residues of the atomic model have larger B-factors at 200 $Å^2$ indicating a higher degree of flexibility than the central helices. Together, helices α1-α4 constitute the elongated four-helix core of the PspA molecules that form the wall of the tubular rod structure via a brick-like stacking. A total of 10.19 subunits are wound in a right-handed manner to form a single 360º turn with a pitch of 30 Å to make up this polar helical assembly consisting of two unique ends (**Figure 2H**). The top view of the assembly reveals that the PspA core helices are arranged like the diaphragm of an iris aperture pointing to the outside of the rod (**Figure 2I**) while the amphipathic paddle helix α5 at the C-terminus emanates from the wall to the outside of the helical rod (**Figure 2J**). Interestingly, at both ends of the PspA core, first the tip of the hairpin between helix α1 and α2 (70-90) and second at the opposite end of helix α4 (167-180), we find highly conserved (>90 % identity) residues among the PspA/IM30 family of proteins (**Figure 2K, Figure S3**) highlighting the evolutionary importance of these intersubunit stabilizing residues. In order to validate the critical importance of these residues, we mutated A75 and A78 and analyzed the PspA_A75S/A78S preparations using negative staining EM. The grids revealed proteinaceous material and showed that the mutant is not able to form rod structures (**Figure S4**). Next, we computed the Coulomb potential of the atomic model PspA assembly. While the lumen and outer surface contains no preferred surface charge, we found that both ends show opposite charges with a basic and acidic surface, respectively (**Figure 2L**), resulting in a polar assembly that has very different binding surfaces at each end of the assembly.

PspA shares the basic domain architecture with ESCRT-III proteins

Based on the here determined cryo-EM structure of PspA, we found one particular structural feature, *i.e.* the helix α1/α2 hairpin packing against a perpendicular helix α5, reminiscent of previously resolved structures of ESCRT-III proteins, which is a well-characterized primarily eukaryotic family of membrane-remodeling proteins. Therefore, we closer examined their apparent similarity by sequence alignment and compared cyanobacterial PspA and IM30 proteins with yeast Vps24 as well as human IST1 and CHMP1B (**Figure 3**), for which high-resolution cryo-EM structures have been determined. Interestingly, there are several stretches that show high sequence agreement (Quality score >4, **Figure S5A**). Furthermore, we focused our analysis on the α1/α2 hairpin region and found that structural superposition yields CA RMSDs with *Eco*PspA (PDB-ID 4WHE, (Osadnik et al., 2015)), IST1 (PDB-ID 6TZA, (Nguyen et al., 2020)), CHMP1B (PDB-ID 6TZ9, (Nguyen et al., 2020)) and Vps24 (PDB-ID 6ZH3, (Huber et al., 2020)) reporting average RMSD values of 1.6 Å, 2.3 Å, 2.2 Å and 1.8 Å, respectively (**Figure S5B**). CHMP1B, Vps24 and PspA adopt elongated conformations, whereas IST1's structure was determined as a compact fold (**Figure 4A**). The corresponding resolved higher-order structures show that all of their assemblies remain unique. IST1/CHMP1B and PspA organize in tubular structures of 260 Å and 200 Å in diameter, respectively (**Figure 4B**). By contrast, homopolymeric yeast Vps24 has been shown to form filaments rather than tubular structures (Ghazi-Tabatabai et al., 2008). However, the fundamental organization of the α-helices remains conserved between all ESCRT-III proteins whereas helix-to-helix loops vary in their precise angular linkage. Nevertheless, common to all structures is that the C-terminal helix α5 packs approx. perpendicularly against the α1/α2 hairpin motif (**Figure 4C**). Based on the identified similarities between primary, secondary and tertiary structure between the here determined bacterial PspA cryo-EM structure and members of the eukaryotic ESCRT-III family, PspA may have shared evolutionary ancestry with ESCRT-III proteins.

PspA mediates fusion of small vesicles into large membrane vesicles

Based on the observed structural homology of PspA with ESCRT-III proteins, we wanted to establish whether PspA has a membrane remodeling activity in analogy to the ESCRT proteins. Therefore, we

incubated PspA rods with small unilamellar (SUVs) vesicles prepared from *E. coli* polar lipid extract (EPL) and analyzed the mixture using cryo-EM. As expected, in the SUV control we visualized a population of small vesicles with 20 - 200 nm diameter (**Figure 5A**). Vesicles show strong contrast in cryo-EM images due to the unilamellar phospholipid bilayer, and thus, morphological changes can be easily monitored. In the cryo-micrographs of the PspA lipid mixture, PspA rods in solution as well as a large fraction of vesicles with increased diameters of up to 1.2 µm were observed (**Figure 5B**). Bilayer perimeter measurements indicate a 5-fold increase of membrane perimeter upon addition of PspA rods, suggesting on average a fusion of at least five smaller vesicles into one large vesicle. The large vesicles in the PspA mixture are often round-shaped and not fully surrounded by a continuous bilayer. Instead, often the lipid bilayer appears to be interrupted by "fuzzy" zones that have PspA protein coats as well as PspA rods associated with the membrane (**Figure 5C**, **Figure S6**). Furthermore, for large vesicles the peak-to-peak separation of the bilayer increased from 2.4 to 5.5 nm measured in class averages (**Figure S7**) when compared with the lipid samples alone (**Figure 5D**). The peak shape and width indicate that the 5.5 nm peak-to-peak distance indeed corresponds to the two bilayer leaflets rather than to a double bilayer structure. Additional micrographs of large unimellar vesicles (LUVs) or the LUV/PspA mixture confirm the observation of an increased leaflet separation of 5.7 nm for fused vesicles (**Figure S8**), and also smaller oligomeric ring structures attached to the membrane surface are commonly observed (**Figure S6**). By contrast, the fuzzy zones are present in smaller as well as larger vesicles and appear to be devoid of an intact lipid bilayer. Thus, they may constitute hot spots of (dissociated) PspA rods mediating vesicle fusion into larger µm-sized liposomes (**Figure 5E and 5F**). Together with the observed structural ESCRT-III homology, the PspA lipid-mixing experiments demonstrate that PspA is capable of mediating vesicle fusion, and can, therefore, be considered a *bona fide* member of the ESCRT-III family of membrane remodeling proteins.

Discussion

The propensity of PspA to form higher-order structures has been shown early on (Hankamer et al., 2004; Kobayashi et al., 2007), yet how oligomerizations contributes to the basic physiological PspA function of

maintaining membrane integrity remained uncertain. Here, we determined the 3.6 Å resolution cryo-EM structure of PspA rod assemblies. We found that PspA assembles into 20-nm wide helical tubes. The wall of the tube is formed by stacking of overall elongated PspA molecules, consisting of a four-helix core of α-helices α1-α4 and the C-terminal amphipathic α-helix projecting to the outer solvent. The structure also revealed a striking similarity to ESCRT-III proteins, which is supported by analyses on several levels of structural organization, including primary, secondary and tertiary structure motifs. Eukaryotic ESCRT proteins are known to assemble in homopolymeric or heterooligomeric complexes that have been shown to mediate membrane remodeling processes in eukaryotic cells, including membrane repair and/or membrane sealing (Takahashi et al., 2018; Vietri et al., 2015; Zhen et al., 2020; Zhu et al., 2017) as well as multivesicular body formation (Katzmann et al., 2001) and viral budding (Garrus et al., 2001). Therefore, we reconstituted PspA rods with lipid vesicles and observed that PspA interacts with the lipid bilayer and mediates fusion of small vesicles into larger µm-sized structures. Given the agreement between structural and functional properties of the PspA molecule, we here identified PspA as a bacterial member of the evolutionary conserved ESCRT-III superfamily of membrane remodeling proteins.

Similar to ESCRT proteins, PspA monomers have an elongated structure with a four-helix core. Yet, in contrast to ESCRT-III proteins, the predicted N-terminal helix α0 was not found to be ordered in our structure. This observation is supported by recent analyses of the isolated N-terminal *Eco*PspA(1-24) fragment using CD spectroscopy, demonstrating that this stretch is disordered in solution but has an increased α-helix content upon binding to membrane surfaces (McDonald et al., 2017). For IM30 and *Eco*PspA, removal of the N-terminal helix affects the equilibrium between monomers, ring or rod structures (Jovanovic et al., 2014; Thurotte and Schneider, 2019), suggesting a central role of the N-terminal helix α0 for formation of defined oligomers. The physiological importance of ring *vs*. rod structures remains an open question, as these structures have not been observed in their native context yet. Using *in vivo* fluorescence microscopy, IM30 and PspA were shown to form dynamic localized *puncta* at curved membrane regions of *Synechocystis* and *E. coli* cells (Gutu et al., 2018; Jovanovic et al., 2014), which is consistent with rings, transient rod or other higher-order structures (Junglas and Schneider, 2018; Siebenaller et al., 2019).

Furthermore, the equilibrium and precise amount of rings and/or rod structures appears to differ between different IM30's and PspA's, as well as between species (Siebenaller et al., 2019). Structurally, rods and rings are closely related, and conversion can be easily envisioned by accommodating small angular changes in subunit-subunit interactions.

Due to revelation of PspA as a member of an ESCRT-III superfamily, we wondered whether there are more similarities beyond the identified structural homology. Initial biochemical characterization of PspA demonstrated already that it is not a typical soluble protein but has an inherent propensity to form higher-order structures (Hankamer et al., 2004; Male et al., 2014; Standar et al., 2008) consistent with the characteristics of many ESCRT-III proteins. Purified ESCRT-III proteins are known to assemble into a variety of large EM-observable structures, amongst them strings, rings, coils, sheets, filaments and domes (Bodon et al., 2011; Ghazi-Tabatabai et al., 2008; Lata et al., 2008). Due to the large number of isoforms of eukaryotic ESCRT-III proteins, the complexity of assembling hetero-complexes is significantly increased, and multiple combinations have been investigated (Henne et al., 2011; Huber et al., 2020; Pfitzner et al., 2020). A structural motif of striking similarity found in PspA as well as in eukaryotic ESCRT structures is the perpendicular packing of helix α5 against the α1/α2 hairpin (see **Figure 4**). In fact, when highly conserved residues (**Figure 2K**) in the loop of connecting the α1/α2 hairpin are mutated, assembly of super-complexes is impaired (**Figure S4**). While these functionally critical contacts have been probed by a series of experimental approaches in ESCRT-III proteins (Bajorek et al., 2009), various modes of helix α5 association have been found, either folding back to its own hairpin (IST1, PDB-ID 6TZA), associating with a domain-swapped dimer (Vps24, PDB-ID 6ZH3) or with neighbors within a helical assembly (CHMP1B (PDB-ID 6TZ9) and PspA). Additionally, helix α4 establishes important intersubunit contacts in the central core of the polymers, which is reflected in a stretch of residues with properties conserved between PspA/IM30 and ESCRT III proteins (**Figure 3**). Accordingly, mutation of the aFErmE cluster **(Figure 2K)** as part of this stretch in the *Syn*IM30 protein also resulted in impaired formation of super-oligomeric complexes (Heidrich et al., 2016; Saur et al., 2017). It is worth to note that the predicted helix α6 of eukaryotic ESCRT-III and IM30 is not evolutionary conserved in PspA and it also has not been observed in

any of the determined polymeric structures of ESCRT-III proteins. A functional property that is conserved between *Eco*PspA and ESCRT-III is the known interaction of two AAA-ATPases PspF and Vps4, respectively. *Eco*PspF and *Eco*PspA have been shown to form a hetero-dodecamer that lead to disassembly of larger PspA multimers into smaller oligomers (Joly et al., 2009). Similarly, ESCRT-III Vps24 filaments fused C-terminally with the MIT domain motif could also be disassembled by Vps4 (Ghazi-Tabatabai et al., 2008). Furthermore, Vps4 was shown to mediate assembly as well as disassembly of ESCRT-III complexes and thereby contributing to membrane remodeling (Maity et al., 2019).

Despite the observed matching structural organization of PspA and ESCRT-III proteins, we further assessed whether PspA and ESCRT-III proteins share functional similarities. Consistent with the proposed function of ESCRT-III being involved in membrane remodeling processes, PspA rods co-incubated with SUVs showed membrane remodeling activity. Cryo-EM images revealed two noteworthy details: PspA binding to membrane surfaces induced a leaflet separation to 5.5 nm and the appearance of µm sized liposomes, presumably as a result of PspA-mediated vesicle fusion. The observed widening of the lipid bilayer likely results from the formation of a PspA carpet on the membrane surface, as recently described for IM30 (Junglas et al., 2020), or previously referred to as clathrin-like network structure in *Eco*PspA preparations (Standar et al., 2008). Membrane adhesion and partial incorporation of PspA molecules into the membrane likely lead to the here observed thickening of the lipid bilayer. Interestingly, it has been shown previously that membrane adhesion of *Syn*IM30 goes along with a bilayer phase transition from the fluid towards the gel phase (Heidrich et al., 2016; Hennig et al., 2015), which is also associated with bilayer thickening. Nevertheless, lipid phase separation alone has recently been observed to cause not more than one nm thickening of a lipid bilayer depending on the bilayer composition (Cornell et al., 2020; Heberle et al., 2020), a value several times lower to the here determined increase in the lipid bilayer thickness. Binding of influenza M1 protein to LUVs, however, was shown to effectively double the detectable bilayer thickness visualized using cryo-EM (Dahmani et al., 2019). The observed bilayer structures could represent a protected form of the lipid bilayer minimizing, for instance, leakage of protons under imposed membrane stress conditions (Kobayashi et al., 2007). Electrostatic surface analysis of the PspA rod structure reveals

an acidic and a basic end that may be responsible for promoting the observed effects. The ends could provide a rational for PspA's observed preference of binding to negatively charged membrane surfaces (Kobayashi et al., 2007; McDonald et al., 2015, 2017). Furthermore, the imaged liposomes show "fuzzy zones" devoid of any visible lipid bilayer but with a high PspA density, often with PspA rods attached to the vesicle surface. The observed sizes of the fuzzy zones are sufficiently large to accommodate smaller vesicles for fusion with the liposome or other solvent content. These vesicle openings are reminiscent of a toroidal pore zone proposed for amphipathic antimicrobial peptides (Brogden, 2005), where at places with high protein concentration PspA likely pulls lipid head groups inwards to line an inner pore wall, and thus, the resulting pores are lined with both PspA and lipids. This way, high local concentrations of PspA can make up a porous zone where PspA molecules lines hydrophobic as well polar stretches of the lipid molecules and thereby interrupting the continuity of the lipid bilayer. In agreement with the here observed formation of porous zones are previous experiments performed with IM30, which demonstrated that the IM30 interaction with membranes disturbs the bilayer in such a way that quencher molecules can enter liposomes (Hennig et al., 2015). It appears to be likely that fuzzy zones are transient structures whereas the widened bilayers are the final product of a fusion process and make up the bulk of the observed membranes of large vesicles. The images of the fuzzy zone contain a grainy texture suggestive of floating PspA molecules dissociated from the rod into smaller units such as rings. Observed flat washer or ring structures would maintain the required end-on basic surfaces to interact with the lipid headgroups while also having amphipathic N and C-terminal paddle helices available for additional lipid interactions. In support of this argument, IM30 larger oligomers were already shown to mediate membrane fusion, and the first helix N-terminus as well as the last helix at the C-terminal are critical for lipid interaction (Hennig et al., 2015, 2017). Interestingly, the fusogenic activity of IM30 could be established using solely the isolated helix α1/α2 hairpin structure (Thurotte and Schneider, 2019), suggesting that in our full-length PspA rod, helix α5 is masking the fusogenic core. In a putative PspA ring structure, helix α1/α2 hairpins will be pointing to the outside of the ring. Noteworthy, our PspA preparations revealed a significant variation of the diameters of the rods. This structural flexibility may be an important property of PspA to accommodate different bilayer intermediate configurations during

the lipid fusion process. Whether PspA's fusion activities are topologically equivalent and compatible with the proposed activities of the ESCRT proteins remains to be established. In contrast to lipid reconstitutions mediated by several eukaryotic ESCRT proteins, a homo-oligomer of PspA alone is already capable of inducing large-scale changes to liposome morphology and thereby represents a minimal bacterial membrane remodeling system. Yet, it is important to identify further mechanistic details of structural intermediates of this membrane remodeling system responsible for maintaining bacterial membrane integrity, which can then be transferred to the eukaryotic ESCRT-III system.

Methods

Expression and purification of PspA

PspA (slr1188) of *Synechocystis* sp. PCC 6803 was heterologously expressed in *E. coli* BL21 (DE3) cells in LB medium using a pRSET6 plasmid. Cells were resuspended in lysis buffer (50 mM sodium phosphate, 300 mM NaCl, pH 7.6) supplemented with a protease inhibitor cocktail (Sigma) and lysed in a cell disruptor (TS Constant Cell disruption systems 1.1 KW; Constant Systems). The lysate was cleared by centrifugation for 15 min at 5000 g. The cleared lysate was incubated over night at 4 ºC to allow formation of filaments. Filaments were pelleted by centrifugation for 15 min at 5000 g. The pellet was resuspended in 50 mM sodium phosphate, 1000 mM NaCl at pH 7.6. The resulting suspension was concentrated by ultracentrifugation (Vivaspin centrifugal filter units MWCO 10 kDa) and washed thoroughly with 10 mM sodium phosphate pH 7.6. The crude filament extract was further purified by differential centrifugation: large particles and aggregates were sedimented by centrifugation for 20 min at 20,000 g; smaller filaments by centrifugation for 60 min at 49,000 g. As a final polishing step, the filaments were diluted and incubated with 0.5% Triton X-100 overnight. Again, large particles and aggregates were removed by low speed centrifugation for 60 min at 20,000 g; filaments were pelleted and washed twice with 10 mM sodium phosphate pH 7.6.

Lipid reconstitution

Chloroform dissolved *E. coli* polar lipid (EPL) extract was purchased from Avanti polar lipids. EPL lipid films were produced by evaporating the solvent under a gentle stream of nitrogen and vacuum desiccation overnight. The lipid films were rehydrated in 10 mM sodium phosphate pH 7.6 by shaking for 30 mins at 37 ºC. The resulting liposome solution was subjected to five freeze-thaw cycles, combined with sonication at 37 ºC in a bath sonicator. SUVs (small unilamellar vesicles) or LUVs (large unilamellar vesicles) were generated by extrusion of the liposome solution through a porous polycarbonate filter (50 nm or 400 nm pores). For membrane interaction studies, PspA filaments (0.8 mg/mL) were incubated with EPL vesicles (5 mg/mL) for at least 2 h at room temperature. PspA lipid mixtures were analyzed by cryo-EM.

Negative-staining electron microscopy

For negative-staining electron microscopy, 5 µL sample was applied to glow-discharged (PELCO easiGlow Glow Discharger, Ted Pella Inc.) continuous carbon grids (Protochips Inc.) and incubated for 1 min. The sample was blotted, washed with water and stained with 5 µL 2% uranyl acetate using the droplet technique. The samples were imaged in a 120 kV FEI Tecnai 12 electron microscope (ThermoFischer Scientific/FEI) equipped with a TVIPS TemCam-F416 4K CCD camera (TVIPS GmbH) at an underfocus of 0.5 to 1.5 µm.

Electron cryo-microscopy

Samples for the full high-resolution dataset of PspA filaments were prepared by applying 3 µL PspA filaments (~7.9 mg/mL) to glow-discharged (PELCO easiGlow Glow Discharger, Ted Pella Inc.) Quantifoil grids (R1.2/1.3 Cu 200 mesh, Electron Microscopy Sciences). The grids were plunge-frozen using a ThermoFisher Scientific Vitrobot Mark IV set to 90% humidity at 10 ºC. A total of 8,342 micrographs were recorded on a 200 kV Talos Arctica electron microscope equipped with a Gatan K3 detector operated by SerialEM (Mastronarde, 2005). Micrographs were collected as 50-frame movies in superresolution mode at 0.419 Å/pixel and a cumulative dose of 50 $e^{-}/Å^{2}$ and a nominal underfocus of 0.2 to 2.3 µm. Samples for an initial cryo-electron microscopy dataset used for symmetry determination were prepared on Lacey Carbon grids (Electron Microscopy Sciences) and imaged using a Titan Krios (300 kV, FEG) cryo-electron

microscope (FEI/Thermo Fischer Scientific), equipped with a Gatan Quantum K2 energy-filtered direct detector. A total of 936 micrographs with a pixel size of 1.35 Å were collected at an underfocus range from 0.8 to 2.6 µm. For cryo-EM of the PspA-liposome mixtures, 3 µL sample were applied to glow-discharged (PELCO easiGlow Glow Discharger, Ted Pella Inc.) lacey-carbon grids (Electron Microscopy Sciences) and manually blotted at the back side of the grid. Plunge-freezing was performed using a in a ThermoFisher Scientific Vitrobot Mark IV, set at 100% humidity and 22 °C temperature. Samples were imaged on a 200 kV Talos Arctica electron microscope equipped with a CETA camera at a pixel size of 2.53 Å/pixel.

Image processing and helical reconstruction

The detailed image processing workflow is presented in **Figure S1**. In order to determine the symmetry parameters, a small dataset of 936 micrographs was utilized (Titan Krios/K2) and PspA filaments were picked manually in RELION 3.0 (Zivanov et al., 2018) and segmented with a step size of 35 Å into 39,600 windows (Test Dataset A, **Figure S1**). The segments were subjected to two rounds of 2D classification. Only classes showing clear secondary structure features and consistent widths were selected. The helical symmetry was determined by analyzing layer lines in the power spectra of the best 2D class and several possible symmetry solutions were obtained using SEGCLASSRECONSTRUCT from the SPRING package (Desfosses et al., 2014). Those symmetry solutions were tested systematically in RELION 3.0 (Zivanov et al., 2018). Using the initial symmetry parameters of 30 Å pitch with 10.25 units per turn, the refinement yielded a map with secondary structure features at 7.3 Å resolution whereas other solutions did not. This initial model was further refined by two rounds of 3D classifications in RELION 3.0. This procedure resulted in an intermediate map of 6.1 Å resolution (FSC=0.143) and refined helical symmetry parameters with a 30.1 Å pitch and 10.19 units per turn corresponding to 2.9 Å rise and 35.3° rotation.

Acquired frames of the full 8,342 micrograph dataset (Talos Arctica/K3) **(Figure S1**) were preprocessed in WARP by binning to the physical pixel size of 0.839 Å/pixel, frame alignment and correcting for beam-induced motion and stage drift (Tegunov and Cramer, 2019). A subset of the resulting micrographs was subjected to manual filament tracing using E2HELIXBOXER (Ludtke, 2016). Manually traced filaments

were used for neural network training and subsequent automated tracing with crYOLO 1.5 (Wagner et al., 2019, 2020). This way, a total of 55,800 rods were detected. After contrast-transfer function (CTF) determination of the micrographs with CTFFIND 4.1 (Rohou and Grigorieff, 2015) and selection of micrographs based on ice quality and image drift (8,257 micrographs), 1.5 million segments (à 450 pixel dimension, at a step size of seven asymmetric units given the 3 Å rise) were extracted from these rods in RELION 3.0 (Zivanov et al., 2018). In a first round of 2D classification, junk particles and classes showing segments with widths >23 nm and <19 nm were discarded and only classes showing clear secondary structure features and power spectra were chosen for further processing (Dataset B, 334,000 segments, **Figure S1**). A simulated helical cylinder was created from the symmetry parameters (2.9 Å rise and 35.2° rotation obtained from Test Dataset A) and used as a reference for 3D classification. This initial reference was further refined by several rounds of 3D classification and subsequent 3D refinement. Finally, one 3D class resulted in a map showing clear sidechain-patterning in the α-helices at 4.7 Å resolution (19,900 segments). The segments of this class were subjected to multiple rounds of per-particle CTF refinement, Bayesian polishing and 3D auto-refinement focusing on the central 30% of the cylinder using a mask. Fourier shell correlation (FSC) curves were calculated within the mask containing the central 30% of the density and local resolutions were determined using RELION's implementation and rendered in ChimeraX (Goddard et al., 2018). The final map was determined to have a global resolution of 3.6 Å (FSC=0.143) (helical symmetry: 2.9 Å rise and 35.3° twist).

Cryo-EM map interpretation and model building

The handedness of the final reconstruction was validated by rigid-body fitting the X-ray structure of the *Eco*PspA hairpin structure (Osadnik et al., 2015) (PDB model 4WHE) by Chimera (Pettersen et al., 2004). The 3D reconstruction was B-factor sharpened (B= -98 $Å^2$) in RELION 3.0 (Zivanov et al., 2018), autosharpened in *phenix.auto_sharpen* (Liebschner et al., 2019; Terwilliger et al., 2020) in Phenix 1.16-3549 and FDR-FSC filtered using SPOC (Beckers and Sachse, 2020). The resulting three maps were used for *de novo* model building in Coot 0.9 (Emsley et al., 2010) for residues 22 - 217. Refinement was

performed in *phenix.real_space_refine* (Afonine et al., 2018a) against the *phenix.auto_sharpen* map after symmetry neighbors were created with *phenix.apply_ncs* (Helical 35.3°; 2.9 Å) using default parameters. After two cycles of refinement and manual inspection, the final model was validated in *phenix.validation_cryoem* (Afonine et al., 2018b) (Table 1). The Coulomb potential of the PspA 10-mer was calculated in Chimera using the built-in "Coulombic Surface Coloring" routine with standard settings. The resulting electrostatic potential grid was sampled on the surface of the refined PspA map in ChimeraX. Structure rendering was done in ChimeraX or Chimera (Goddard et al., 2018; Pettersen et al., 2004). Image processing, helical reconstruction and model building was completed using SBGrid-supported applications (Morin et al., 2013).

Image analysis of membranes

To quantitatively assess the size and size changes of EPL vesicles upon addition of PspA, minimum and maximum widths of liposomes, as well as their perimeter, were measured using ImageJ (Rueden et al., 2017). To determine the bilayer leaflet distance, 2D classification of bilayer segments was employed. The bilayer was traced manually in RELION 3.0 using the filament-picking option (Zivanov et al., 2018). From these traces, segments were extracted every 20 Å with a box size of 100 px at 2.53 Å/pixel yielding 9,963 segments of vesicles only, 8,571 segments of small vesicles and PspA and 17,056 segments of large vesicles and PspA. Bilayer segments were CTF corrected based on micrograph CTF determination (CTFFIND 4.1 (Rohou and Grigorieff, 2015) and segment images of these groups were subjected to 2D classification in RELION 3.0 (Zivanov et al., 2018) (**Figure S7 and S8**). Relative intensity profiles of the class averages were analyzed in OriginPro 2020b using the "Multiple Peak Fit" tool with a Gauss peak function. The leaflet distance *d* was measured as the distance between two peak centers in each class average. Leaflet distances were averaged within each group.

Acknowledgments

This work was funded by the Max-Planck Graduate Center at the Max Planck institutes and the University of Mainz. This work has been supported by iNEXT, grant number 653706, funded by the Horizon 2020 program of the European Union.

Author contributions

B.J., D.S. and C.S. designed research. B.J. purified the protein and together with M.C. prepared cryo-EM samples. J.O.O. and T.S. operated the electron microscopes. B.J. and S.T.H. determined the cryo-EM structure. D.M. and B.J. built the refined atomic model. R.H. performed mutation experiments. B.J. performed lipid-mixing experiments. B.J., D.S., and C.S. wrote the manuscript with input from all authors.

Declaration of interests

The authors disclose any financial or non-financial conflict of interest.

Data and materials availability

All data needed to evaluate the conclusions in the paper are present in the paper and/or the Supplementary Information. The EMDB accession numbers for the cryo-EM map and PspA model are EMD-11698 and PDB-ID 7ABK.

References

Afonine, P.V., Poon, B.K., Read, R.J., Sobolev, O.V., Terwilliger, T.C., Urzhumtsev, A., and Adams, P.D. (2018a). Real-space refinement in PHENIX for cryo-EM and crystallography. Acta Cryst D *74*, 531–544.

Afonine, P.V., Klaholz, B.P., Moriarty, N.W., Poon, B.K., Sobolev, O.V., Terwilliger, T.C., Adams, P.D., and Urzhumtsev, A. (2018b). New tools for the analysis and validation of cryo-EM maps and atomic models. Acta Cryst D *74*, 814–840.

Aseeva, E., Ossenbühl, F., Eichacker, L.A., Wanner, G., Soll, J., and Vothknecht, U.C. (2004). Complex formation of Vipp1 depends on its α-helical PspA-like domain. Journal of Biological Chemistry *279*, 35535–35541.

Ashkenazy, H., Abadi, S., Martz, E., Chay, O., Mayrose, I., Pupko, T., and Ben-Tal, N. (2016). ConSurf 2016: an improved methodology to estimate and visualize evolutionary conservation in macromolecules. Nucleic Acids Res *44*, W344–W350.

Bajorek, M., Morita, E., Skalicky, J.J., Morham, S.G., Babst, M., and Sundquist, W.I. (2009). Biochemical analyses of human IST1 and its function in cytokinesis. Mol. Biol. Cell *20*, 1360–1373.

Beckers, M., and Sachse, C. (2020). Adaptive FDR thresholding of Fourier shell correlation for resolution estimation of cryo-EM maps. BioRxiv 2020.03.13.990705.

Bodon, G., Chassefeyre, R., Pernet-Gallay, K., Martinelli, N., Effantin, G., Hulsik, D.L., Belly, A., Goldberg, Y., Chatellard-Causse, C., Blot, B., et al. (2011). Charged Multivesicular Body Protein 2B (CHMP2B) of the Endosomal Sorting Complex Required for Transport-III (ESCRT-III) Polymerizes into Helical Structures Deforming the Plasma Membrane. J. Biol. Chem. *286*, 40276–40286.

Bohuszewicz, O., Liu, J., and Low, H.H. (2016). Membrane remodelling in bacteria. Journal of Structural Biology *196*, 3–14.

Brogden, K.A. (2005). Antimicrobial peptides: pore formers or metabolic inhibitors in bacteria? Nat. Rev. Microbiol. *3*, 238–250.

Bultema, J.B., Fuhrmann, E., Boekema, E.J., and Schneider, D. (2010). Vipp1 and PspA. Communicative & Integrative Biology *3*, 162–165.

Caillat, C., Maity, S., Miguet, N., Roos, W.H., and Weissenhorn, W. (2019). The role of VPS4 in ESCRT-III polymer remodeling. Biochem. Soc. Trans. *47*, 441–448.

Carlton, J.G., and Martin-Serrano, J. (2007). Parallels between cytokinesis and retroviral budding: a role for the ESCRT machinery. Science *316*, 1908–1912.

Cornell, C.E., Mileant, A., Thakkar, N., Lee, K.K., and Keller, S.L. (2020). Direct imaging of liquid domains in membranes by cryo-electron tomography. PNAS *117*, 19713–19719.

Dahmani, I., Ludwig, K., and Chiantia, S. (2019). Influenza A matrix protein M1 induces lipid membrane deformation via protein multimerization. Biosci. Rep. *39*.

Desfosses, A., Ciuffa, R., Gutsche, I., and Sachse, C. (2014). SPRING – An image processing package for single-particle based helical reconstruction from electron cryomicrographs. Journal of Structural Biology *185*, 15–26.

Di Tommaso, P., Moretti, S., Xenarios, I., Orobitg, M., Montanyola, A., Chang, J.-M., Taly, J.-F., and Notredame, C. (2011). T-Coffee: a web server for the multiple sequence alignment of protein and RNA sequences using structural information and homology extension. Nucleic Acids Res *39*, W13–W17.

Emsley, P., Lohkamp, B., Scott, W.G., and Cowtan, K. (2010). Features and development of *Coot*. Acta Crystallogr D Biol Crystallogr *66*, 486–501.

Ford, M.G.J., Mills, I.G., Peter, B.J., Vallis, Y., Praefcke, G.J.K., Evans, P.R., and McMahon, H.T. (2002). Curvature of clathrin-coated pits driven by epsin. Nature *419*, 361–366.

Frost, A., Unger, V.M., and De Camilli, P. (2009). The BAR Domain Superfamily: Membrane-Molding Macromolecules. Cell *137*, 191–196.

Fuhrmann, E., Bultema, J.B., Kahmann, U., Rupprecht, E., Boekema, E.J., and Schneider, D. (2009). The vesicle-inducing protein 1 from Synechocystis sp. PCC 6803 organizes into diverse higher-ordered ring structures. Molecular Biology of the Cell *20*, 4620–4628.

Garrus, J.E., von Schwedler, U.K., Pornillos, O.W., Morham, S.G., Zavitz, K.H., Wang, H.E., Wettstein, D.A., Stray, K.M., Côté, M., Rich, R.L., et al. (2001). Tsg101 and the vacuolar protein sorting pathway are essential for HIV-1 budding. Cell *107*, 55–65.

Gautier, R., Douguet, D., Antonny, B., and Drin, G. (2008). HELIQUEST: a web server to screen sequences with specific -helical properties. Bioinformatics *24*, 2101–2102.

Ghazi-Tabatabai, S., Saksena, S., Short, J.M., Pobbati, A.V., Veprintsev, D.B., Crowther, R.A., Emr, S.D., Egelman, E.H., and Williams, R.L. (2008). Structure and disassembly of filaments formed by the ESCRT-III subunit Vps24. Structure *16*, 1345–1356.

Goddard, T.D., Huang, C.C., Meng, E.C., Pettersen, E.F., Couch, G.S., Morris, J.H., and Ferrin, T.E. (2018). UCSF ChimeraX: Meeting modern challenges in visualization and analysis. Protein Science *27*, 14–25.

Gutu, A., Chang, F., and O'Shea, E.K. (2018). Dynamical localization of a thylakoid membrane binding protein is required for acquisition of photosynthetic competency. Molecular Microbiology *108*, 16–31.

Hankamer, B.D., Elderkin, S.L., Buck, M., and Nield, J. (2004). Organization of the AAA+ Adaptor Protein PspA Is an Oligomeric Ring. Journal of Biological Chemistry *279*, 8862–8866.

Heberle, F.A., Doktorova, M., Scott, H.L., Skinkle, A.D., Waxham, M.N., and Levental, I. (2020). Direct label-free imaging of nanodomains in biomimetic and biological membranes by cryogenic electron microscopy. Proc. Natl. Acad. Sci. U.S.A. *117*, 19943–19952.

Heidrich, J., Wulf, V., Hennig, R., Saur, M., Markl, J., Sönnichsen, C., and Schneider, D. (2016). Organization into higher ordered ring structures counteracts membrane binding of IM30, a protein associated with inner membranes in chloroplasts and cyanobacteria. Journal of Biological Chemistry *291*, 14954–14962.

Henne, W.M., Buchkovich, N.J., and Emr, S.D. (2011). The ESCRT pathway. Dev. Cell *21*, 77–91.

Hennig, R., Heidrich, J., Saur, M., Schmüser, L., Roeters, S.J., Hellmann, N., Woutersen, S., Bonn, M., Weidner, T., Markl, J., et al. (2015). IM30 triggers membrane fusion in cyanobacteria and chloroplasts. Nature Communications *6*.

Hennig, R., West, A., Debus, M., Saur, M., Markl, J., Sachs, J.N., and Schneider, D. (2017). The IM30/Vipp1 C-terminus associates with the lipid bilayer and modulates membrane fusion. Biochimica et Biophysica Acta - Bioenergetics *1858*, 126–136.

Huber, S.T., Mostafavi, S., Mortensen, S.A., and Sachse, C. (2020). Structure and assembly of ESCRT-III helical Vps24 filaments. Science Advances *6*, eaba4897.

Joly, N., Burrows, P.C., Engl, C., Jovanovic, G., and Buck, M. (2009). A lower-order oligomer form of phage shock protein A (PspA) stably associates with the hexameric AAA(+) transcription activator protein PspF for negative regulation. J. Mol. Biol. *394*, 764–775.

Joly, N., Engl, C., Jovanovic, G., Huvet, M., Toni, T., Sheng, X., Stumpf, M.P.H., and Buck, M. (2010). Managing membrane stress: The phage shock protein (Psp) response, from molecular mechanisms to physiology. FEMS Microbiology Reviews *34*, 797–827.

Jovanovic, G., Mehta, P., McDonald, C., Davidson, A.C., Uzdavinys, P., Ying, L., and Buck, M. (2014). The N-terminal amphipathic helices determine regulatory and effector functions of phage shock protein A (PspA) in escherichia coli. Journal of Molecular Biology *426*, 1498–1511.

Junglas, B., and Schneider, D. (2018). What is Vipp1 good for? Molecular Microbiology.

Junglas, B., Orru, R., Axt, A., Siebenaller, C., Steinchen, W., Heidrich, J., Hellmich, U.A., Hellmann, N., Wolf, E., Weber, S.A.L., et al. (2020). IM30 IDPs form a membrane protective carpet upon super-complex disassembly. BioRxiv.

Katzmann, D.J., Babst, M., and Emr, S.D. (2001). Ubiquitin-Dependent Sorting into the Multivesicular Body Pathway Requires the Function of a Conserved Endosomal Protein Sorting Complex, ESCRT-I. Cell *106*, 145–155.

Kobayashi, R., Suzuki, T., and Yoshida, M. (2007). Escherichia coli phage-shock protein A (PspA) binds to membrane phospholipids and repairs proton leakage of the damaged membranes. Molecular Microbiology *66*, 100–109.

Larkin, M.A., Blackshields, G., Brown, N.P., Chenna, R., McGettigan, P.A., McWilliam, H., Valentin, F., Wallace, I.M., Wilm, A., Lopez, R., et al. (2007). Clustal W and Clustal X version 2.0. Bioinformatics *23*, 2947–2948.

Lata, S., Schoehn, G., Jain, A., Pires, R., Piehler, J., Gottlinger, H.G., and Weissenhorn, W. (2008). Helical structures of ESCRT-III are disassembled by VPS4. Science *321*, 1354–1357.

Liebschner, D., Afonine, P.V., Baker, M.L., Bunkóczi, G., Chen, V.B., Croll, T.I., Hintze, B., Hung, L.-W., Jain, S., McCoy, A.J., et al. (2019). Macromolecular structure determination using X-rays, neutrons and electrons: recent developments in Phenix. Acta Cryst D *75*, 861–877.

Lindås, A.-C., Karlsson, E.A., Lindgren, M.T., Ettema, T.J.G., and Bernander, R. (2008). A unique cell division machinery in the Archaea. Proc. Natl. Acad. Sci. U.S.A. *105*, 18942–18946.

Low, H.H., Sachse, C., Amos, L.A., and Löwe, J. (2009). Structure of a Bacterial Dynamin-like Protein Lipid Tube Provides a Mechanism For Assembly and Membrane Curving. Cell *139*, 1342–1352.

Ludtke, S.J. (2016). Single-Particle Refinement and Variability Analysis in EMAN2.1. Meth. Enzymol. *579*, 159–189.

Maity, S., Caillat, C., Miguet, N., Sulbaran, G., Effantin, G., Schoehn, G., Roos, W.H., and Weissenhorn, W. (2019). VPS4 triggers constriction and cleavage of ESCRT-III helical filaments. Science Advances *5*, eaau7198.

Male, A.L., Oyston, P.C.F., and Tavassoli, A. (2014). Self-Assembly of Escherichia coli Phage Shock Protein A. Advances in Microbiology *04*, 353–359.

Manganelli, R., and Gennaro, M.L. (2017). Protecting from Envelope Stress: Variations on the Phage-Shock-Protein Theme. Trends in Microbiology *25*, 205–216.

Mastronarde, D.N. (2005). Automated electron microscope tomography using robust prediction of specimen movements. J. Struct. Biol. *152*, 36–51.

McCullough, J., Clippinger, A.K., Talledge, N., Skowyra, M.L., Saunders, M.G., Naismith, T.V., Colf, L.A., Afonine, P., Arthur, C., Sundquist, W.I., et al. (2015). Structure and membrane remodeling activity of ESCRT-III helical polymers. Science *350*, 1548–1551.

McDonald, C., Jovanovic, G., Ces, O., and Buck, M. (2015). Membrane stored curvature elastic stress modulates recruitment of maintenance proteins pspa and vipp1. MBio *6*, e01188-15.

McDonald, C., Jovanovic, G., Wallace, B.A., Ces, O., and Buck, M. (2017). Structure and function of PspA and Vipp1 N-terminal peptides: Insights into the membrane stress sensing and mitigation. Biochimica et Biophysica Acta - Biomembranes *1859*, 28–39.

Morin, A., Eisenbraun, B., Key, J., Sanschagrin, P.C., Timony, M.A., Ottaviano, M., and Sliz, P. (2013). Collaboration gets the most out of software. ELife *2*, e01456.

Muzioł, T., Pineda-Molina, E., Ravelli, R.B., Zamborlini, A., Usami, Y., Göttlinger, H., and Weissenhorn, W. (2006). Structural basis for budding by the ESCRT-III factor CHMP3. Dev. Cell *10*, 821–830.

Nguyen, H.C., Talledge, N., McCullough, J., Sharma, A., Moss, F.R., Iwasa, J.H., Vershinin, M.D., Sundquist, W.I., and Frost, A. (2020). Membrane constriction and thinning by sequential ESCRT-III polymerization. Nature Structural & Molecular Biology *27*, 392–399.

Osadnik, H., Schöpfel, M., Heidrich, E., Mehner, D., Lilie, H., Parthier, C., Risselada, H.J., Grubmüller, H., Stubbs, M.T., and Brüser, T. (2015). PspF-binding domain PspA1-144and the PspA·F complex: New insights into the coiled-coil-dependent regulation of AAA+ proteins. Molecular Microbiology *98*, 743–759.

Pettersen, E.F., Goddard, T.D., Huang, C.C., Couch, G.S., Greenblatt, D.M., Meng, E.C., and Ferrin, T.E. (2004). UCSF Chimera?A visualization system for exploratory research and analysis. Journal of Computational Chemistry *25*, 1605–1612.

Pfitzner, A.-K., Mercier, V., Jiang, X., Moser von Filseck, J., Baum, B., Šarić, A., and Roux, A. (2020). An ESCRT-III Polymerization Sequence Drives Membrane Deformation and Fission. Cell *182*, 1140-1155.e18.

Praefcke, G.J.K., and McMahon, H.T. (2004). The dynamin superfamily: universal membrane tubulation and fission molecules? Nat. Rev. Mol. Cell Biol. *5*, 133–147.

Rohou, A., and Grigorieff, N. (2015). CTFFIND4: Fast and accurate defocus estimation from electron micrographs. Journal of Structural Biology *192*, 216–221.

Rueden, C.T., Schindelin, J., Hiner, M.C., DeZonia, B.E., Walter, A.E., Arena, E.T., and Eliceiri, K.W. (2017). ImageJ2: ImageJ for the next generation of scientific image data. BMC Bioinformatics *18*, 529.

Samson, R.Y., Obita, T., Freund, S.M., Williams, R.L., and Bell, S.D. (2008). A role for the ESCRT system in cell division in archaea. Science *322*, 1710–1713.

Saur, M., Hennig, R., Young, P., Rusitzka, K., Hellmann, N., Heidrich, J., Morgner, N., Markl, J., and Schneider, D. (2017). A Janus-Faced IM30 Ring Involved in Thylakoid Membrane Fusion Is Assembled from IM30 Tetramers. Structure *25*, 1380-1390.e5.

Siebenaller, C., Junglas, B., and Schneider, D. (2019). Functional Implications of Multiple IM30 Oligomeric States. Front. Plant Sci. *10*.

Siebenaller, C., Junglas, B., Lehmann, A., Hellmann, N., and Schneider, D. (2020). Proton Leakage Is Sensed by IM30 and Activates IM30-Triggered Membrane Fusion. International Journal of Molecular Sciences *21*, 4530.

Standar, K., Mehner, D., Osadnik, H., Berthelmann, F., Hause, G., Lünsdorf, H., and Brüser, T. (2008). PspA can form large scaffolds in Escherichia coli. FEBS Letters *582*, 3585–3589.

Szwedziak, P., Wang, Q., Bharat, T.A.M., Tsim, M., and Löwe, J. (2014). Architecture of the ring formed by the tubulin homologue FtsZ in bacterial cell division. ELife *3*, e04601.

Takahashi, Y., He, H., Tang, Z., Hattori, T., Liu, Y., Young, M.M., Serfass, J.M., Chen, L., Gebru, M., Chen, C., et al. (2018). An autophagy assay reveals the ESCRT-III component CHMP2A as a regulator of phagophore closure. Nature Communications *9*, 2855.

Tegunov, D., and Cramer, P. (2019). Real-time cryo-electron microscopy data preprocessing with Warp. Nature Methods *16*, 1146–1152.

Terwilliger, T.C., Ludtke, S.J., Read, R.J., Adams, P.D., and Afonine, P.V. (2020). Improvement of cryo-EM maps by density modification. BioRxiv 845032.

Theis, J., Gupta, T.K., Klingler, J., Wan, W., Albert, S., Keller, S., Engel, B.D., and Schroda, M. (2019). VIPP1 rods engulf membranes containing phosphatidylinositol phosphates. Scientific Reports *9*, 8725.

Theis, J., Niemeyer, J., Schmollinger, S., Ries, F., Rütgers, M., Gupta, T.K., Sommer, F., Muranaka, L.S., Venn, B., Schulz-Raffelt, M., et al. (2020). VIPP2 interacts with VIPP1 and HSP22E/F at chloroplast membranes and modulates a retrograde signal for *HSP22E/F* gene expression. Plant, Cell & Environment *43*, 1212–1229.

Thurotte, A., and Schneider, D. (2019). The fusion activity of IM30 rings involves controlled unmasking of the fusogenic core. Frontiers in Plant Science *10*, 108.

Thurotte, A., Brüser, T., Mascher, T., and Schneider, D. (2017). Membrane chaperoning by members of the PspA/IM30 protein family. Communicative & Integrative Biology *10*, e1264546.

Vietri, M., Schink, K.O., Campsteijn, C., Wegner, C.S., Schultz, S.W., Christ, L., Thoresen, S.B., Brech, A., Raiborg, C., and Stenmark, H. (2015). Spastin and ESCRT-III coordinate mitotic spindle disassembly and nuclear envelope sealing. Nature *522*, 231–235.

Vothknecht, U.C., Otters, S., Hennig, R., and Schneider, D. (2012). Vipp1: A very important protein in plastids?! Journal of Experimental Botany *63*, 1699–1712.

Wagner, T., Merino, F., Stabrin, M., Moriya, T., Antoni, C., Apelbaum, A., Hagel, P., Sitsel, O., Raisch, T., Prumbaum, D., et al. (2019). SPHIRE-crYOLO is a fast and accurate fully automated particle picker for cryo-EM. Communications Biology *2*, 1–13.

Wagner, T., Lusnig, L., Pospich, S., Stabrin, M., Schönfeld, F., and Raunser, S. (2020). Two particle-picking procedures for filamentous proteins: SPHIRE-crYOLO filament mode and SPHIRE-STRIPER. Acta Cryst D *76*, 613–620.

Waterhouse, A.M., Procter, J.B., Martin, D.M.A., Clamp, M., and Barton, G.J. (2009). Jalview Version 2--a multiple sequence alignment editor and analysis workbench. Bioinformatics *25*, 1189–1191.

Wolf, D., Kalamorz, F., Wecke, T., Juszczak, A., Mäder, U., Homuth, G., Jordan, S., Kirstein, J., Hoppert, M., Voigt, B., et al. (2010). In-depth profiling of the LiaR response of bacillus subtilis. Journal of Bacteriology *192*, 4680–4693.

Zhen, Y., Spangenberg, H., Munson, M.J., Brech, A., Schink, K.O., Tan, K.-W., Sørensen, V., Wenzel, E.M., Radulovic, M., Engedal, N., et al. (2020). ESCRT-mediated phagophore sealing during mitophagy. Autophagy *16*, 826–841.

Zhu, W., Krishna, S., Garcia, C., Lin, C.-C.J., Mitchell, B.D., Scott, K.L., Mohila, C.A., Creighton, C.J., Yoo, S.-H., Lee, H.K., et al. (2017). Daam2 driven degradation of VHL promotes gliomagenesis. ELife *6*, e31926.

Zivanov, J., Nakane, T., Forsberg, B., Kimanius, D., Hagen, W.J.H., Lindahl, E., and Scheres, S.H.W. (2018). RELION-3: new tools for automated high-resolution cryo-EM structure determination. BioRxiv 421123.

Figures

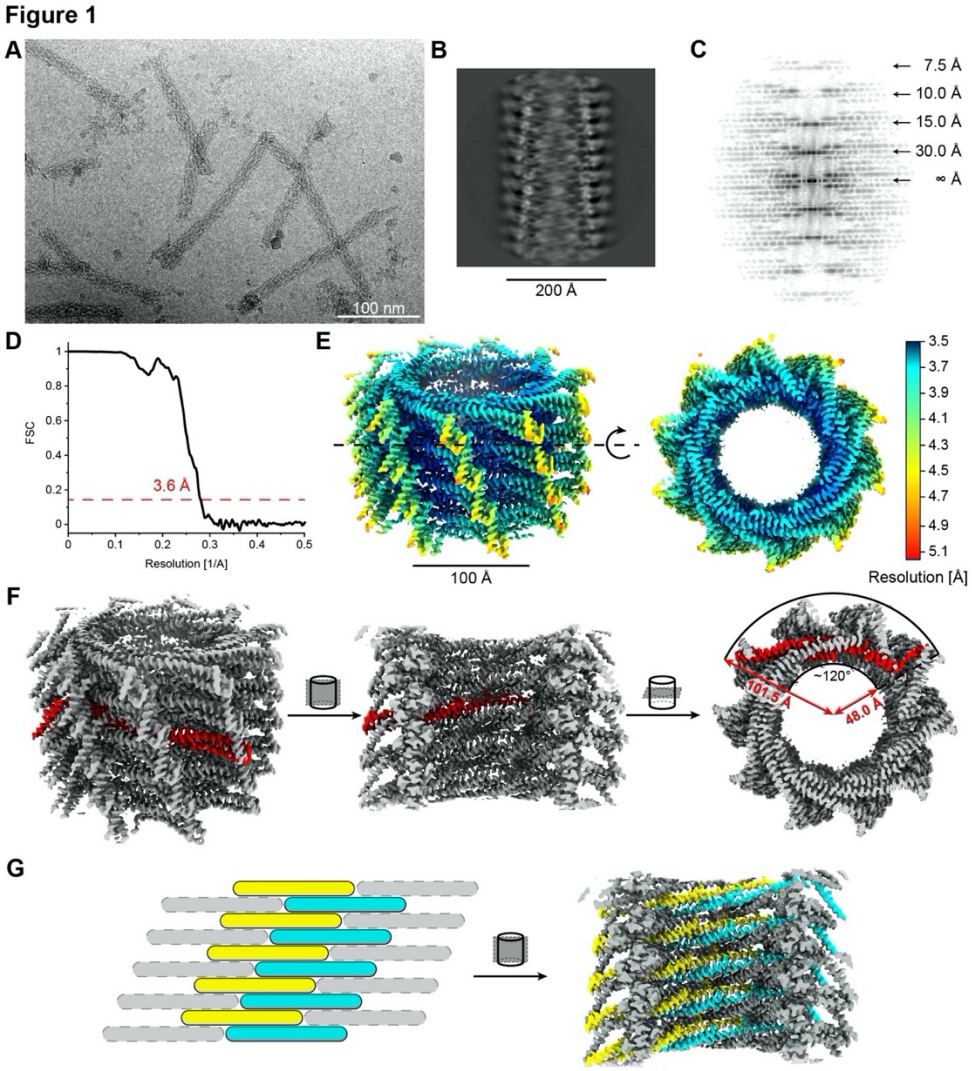

Figure 1: Cryo-EM structure of helical PspA assemblies.

(A) Representative electron cryo-micrograph of PspA rods. (B) Detailed class average of Christmas-tree appearance and (C) corresponding power spectrum indicating layer lines up to 7 Å resolution. (D) Fourier shell correlation supporting 3.6 Å resolution at the 0.143 cutoff. (E) Local resolution estimates are mapped onto the surface of the PspA cryo-EM structure. The resolution varies from 3.5 Å at the inner wall to 4.7 Å at the C-terminal helix. (F) Left: side view of cryo-EM density with a single segmented subunit in red. Center: open cylinder side view. Right: top view. (G) Left: schematic view of subunits stacked like bricks forming a wall. Right: open half-cylinder view of stacked subunits forming the cylinder wall.

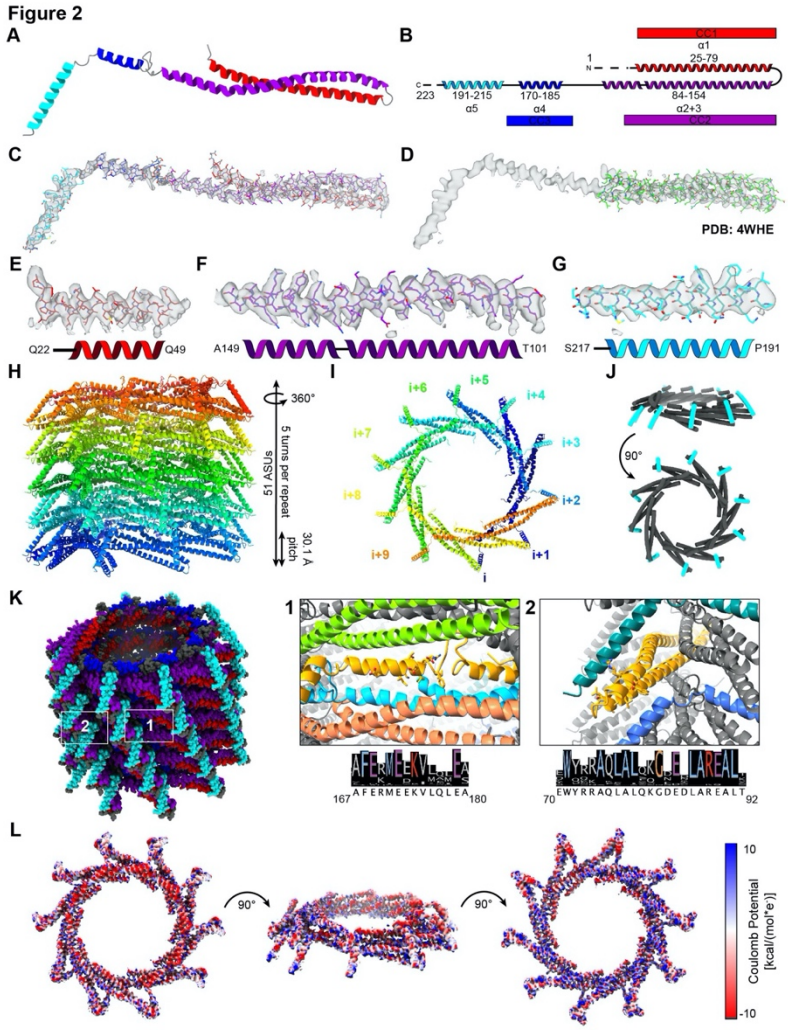

Figure 2: PspA atomic model and architecture of the helical PspA assembly.

(A) Built atomic model of PspA (25-215) with colored α-helices in ribbon presentation (α1: red, α2/α3: purple, α4: blue, α5: cyan) (B) Primary structure with secondary structure overlaid in the same color scheme as in (A). Note that helices were named following the ESCRT-III nomenclature. (C) Segmented cryo-EM density superimposed on built atomic model of PspA. (D) Rigid body fit of the *Eco*PspA (25-141) X-ray structure PDB-ID 4WHE. (E) Density of helix α1. (F) Central helix density with helix α2 and α3. (G) C-terminal helix α5 with poorer density. (H) The rod assembly in side view: elongated monomers (in rainbow colors) assemble to form a right-handed helix of 10.19 subunits per turn, *i.e.* corresponding to a pitch of 30.1 Å. (I) Top view of the assembly corresponding to one turn of stacked monomers i, i+1, i+2 … i+9 (in rainbow colors). (J) Helix α5 (cyan) forms a paddle that emanates from the wall to the outside of the helical

rod. (K) Helical assembly of 51 PspA monomers in sphere representation in the same color scheme as in (A). Detail 1 (residues 167-180) and 2 (residues 70-92) show the structural context of highly conserved residues in PspA (color code rainbow as in H). (L) Electrostatic surface potential of PspA rods. The assembly consists of two unique ends with basic and acidic surfaces.

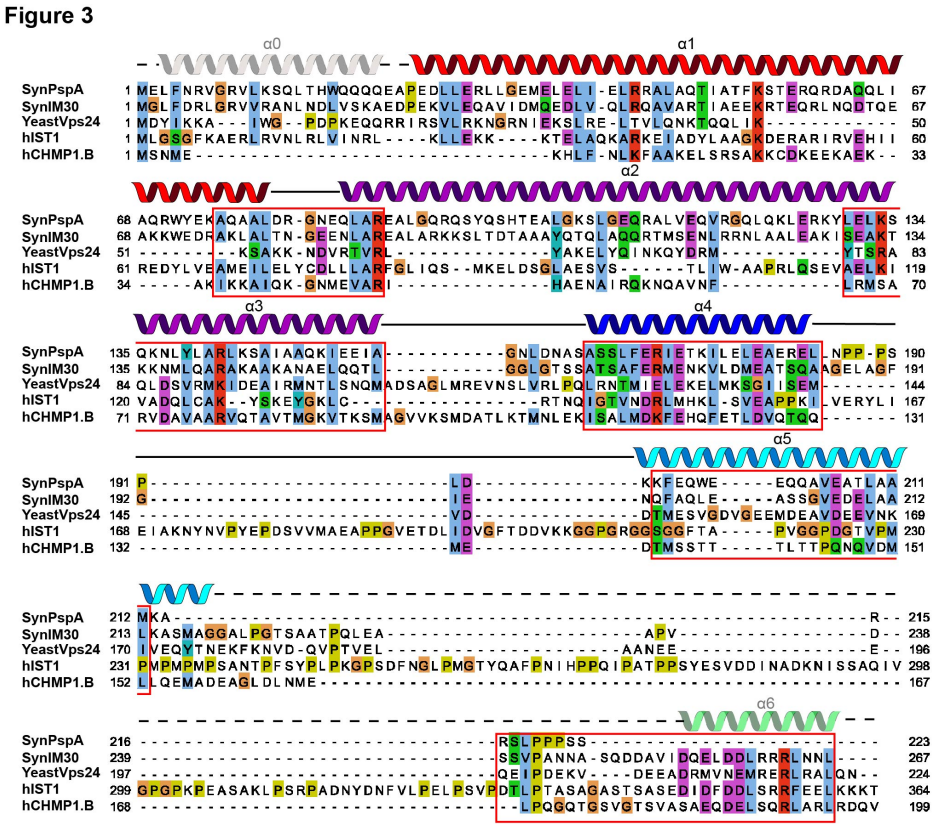

Figure 3: Sequence comparison of PspA/IM30 with ESCRT-III proteins.

Sequence alignment of *Syn*PspA, *Syn*IM30, YeastVps24, humanIST1 and humanCHMP1.B superimposed with the secondary structures according to the ESCRT-III nomenclature. Residues with similarity >30 % are colored according to their properties (ClustalX color scheme). Stretches of high similarity are highlighted with red boxes. Alignment scores for the boxed areas are shown in **Figure S5B**. Sequences were aligned using the T-Coffee webserver (Di Tommaso et al., 2011) and visualized with JalView (Waterhouse et al., 2009).

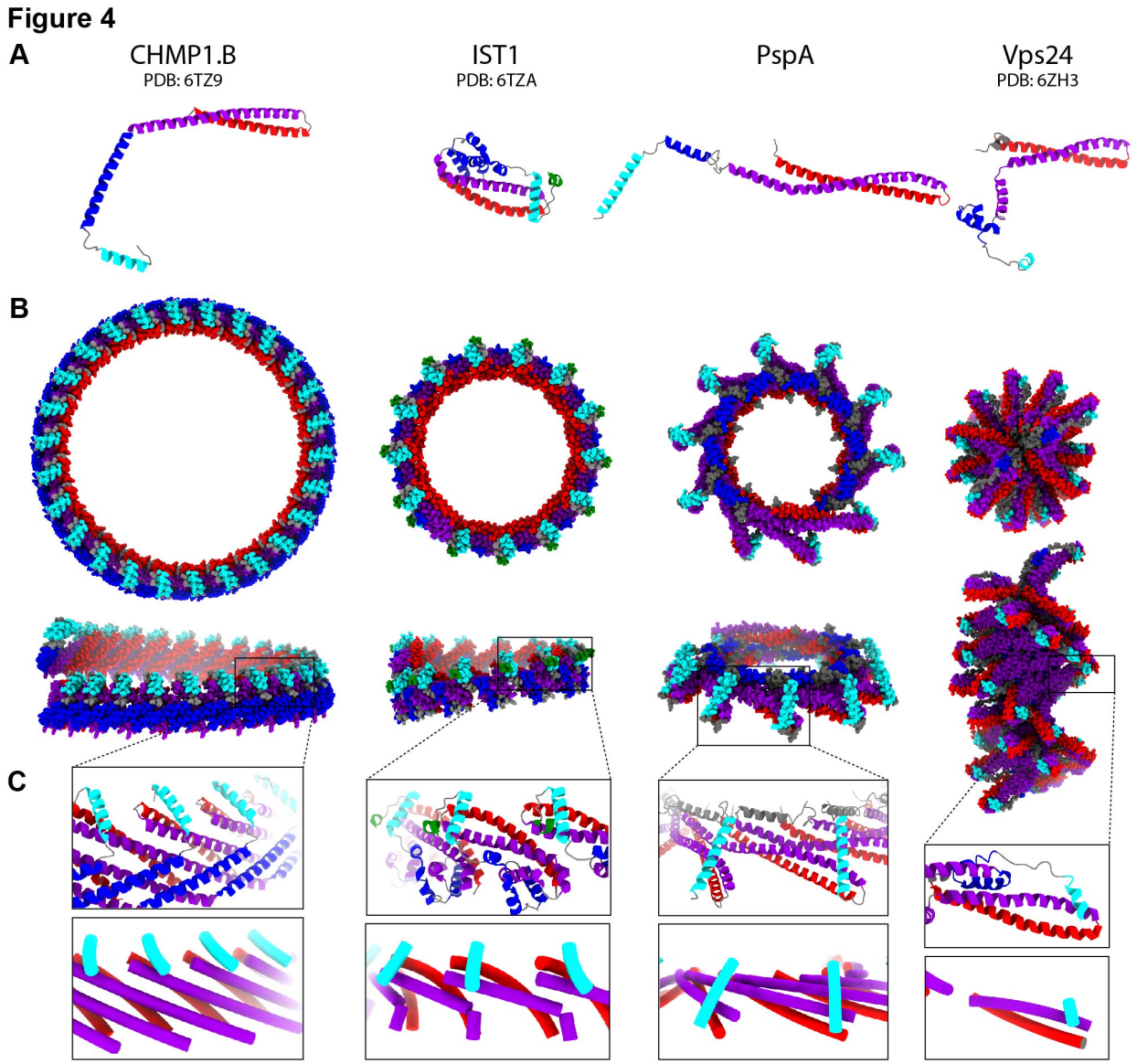

Figure 4: Comparison of the PspA structure with ESCRT-III proteins.

(A) Monomer views of CHMP1.B, IST1, PspA and Vps24 with colored α-helices in ribbon presentation (α1: red, α2/α3: purple, α4: blue, α5: cyan). (B) Helical assemblies of ESCRT-III proteins and PspA in sphere representation with the same coloring scheme as in (A). Upper row: top views, lower row: side views. (C) Details of the ESCRT-III and PspA assemblies showing a conserved motif with helix α5 being packed approx. perpendicularly against the α1/α2 hairpin motif.

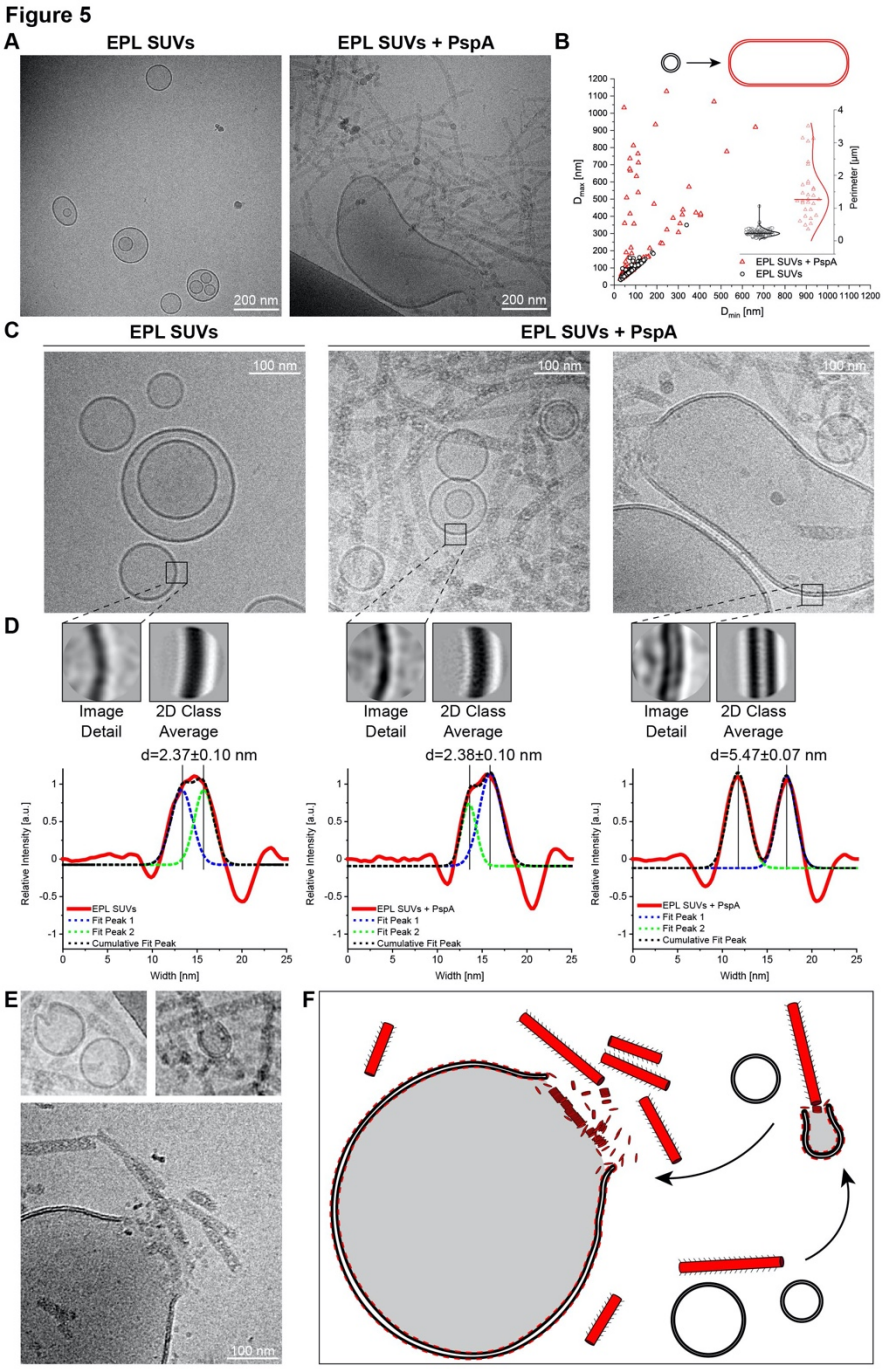

Figure 5: Membrane binding and remodeling by PspA.

(A) Electron cryo-microscopy images of small unilamellar vesicles (SUVs) prepared from *E. coli* polar lipid extract (EPL) alone (left) or incubated with PspA rods (right). (B) Analysis of EPL vesicle dimensions in the presence (red triangles, n=209) and in the absence of PspA (black circles, n=210). (C) EPL forms small

uniform vesicles in the absence of PspA (left), a fraction of unaltered uniform vesicles in the presence of PspA (center) and larger deformed vesicles with a distinct bilayer leaflet separation (right). A representative and diverse gallery of EPL vesicles after incubation with PspA rods is shown in **Figure S6**. (D) Analysis of bilayer leaflet separation *d* in EPL vesicles corresponding to populations from (C). The intensity profiles were extracted from class averages of segmented bilayers (n=5 class averages, errors represent SD). The respective class averages are shown in **Figure S7.** (E) Close-up views of two closed small vesicles (top left), one open vesicle with a horse-shoe shape (top right) and fused large vesicle with a larger fuzzy zone (bottom). (F) Model describing interaction of PspA with membranes based on the cryo-EM image observations. PspA polymers (red rods) contact lipid membranes and disassemble. Dissociated PspA gives rise to "fuzzy" zones at the membrane surface that are putative fusion-active porous zones ready to fuse with smaller vesicles. Finally, after fusion, PspA remains bound to the lipid membrane forming a continuous coat ("carpet") evident by an increased leaflet separation.

Tables

Table 1. PspA cryo-EM structure determination: Details of single-particle cryo-EM and atomic coordinate refinement

Data collection and processing	**PspA**
Magnification	x100,000
Voltage (kV)	200
Electron exposure (e^-/ Å ^{2})	50
Underfocus range (μm)	0.2 - 2.3
Pixel size (Å)	0.8389
Detector	Gatan K3
Symmetry imposed	C1 and helical
Final no. of segments/asymmetric units	19,889/139,223
Helical rise (Å)	2.9
Helical twist (°)	35.3
Global map resolution (Å, FSC = 0.143)	3.6
Local map resolution range (Å)	3.5 - 5.1
Initial model used (PDB code)	-
Model refinement	**PspA**
Model resolution	3.4
CC mask	0.87
Map sharpening B-factor (Å^2)	-98
Model composition	
Nonhydrogen atoms	1574
Protein residues	196
RMSDs	
Bond lengths (Å)	0.004
Bond angles (°)	0.640
Validation	
MolProbity score	1.36
Clashscore	5.35
Rotamer outliers (%)	1.23
Ramachandran plot	
Favored (%)	98.45
Allowed (%)	1.55
Disallowed (%)	0.00

Supplemental Information

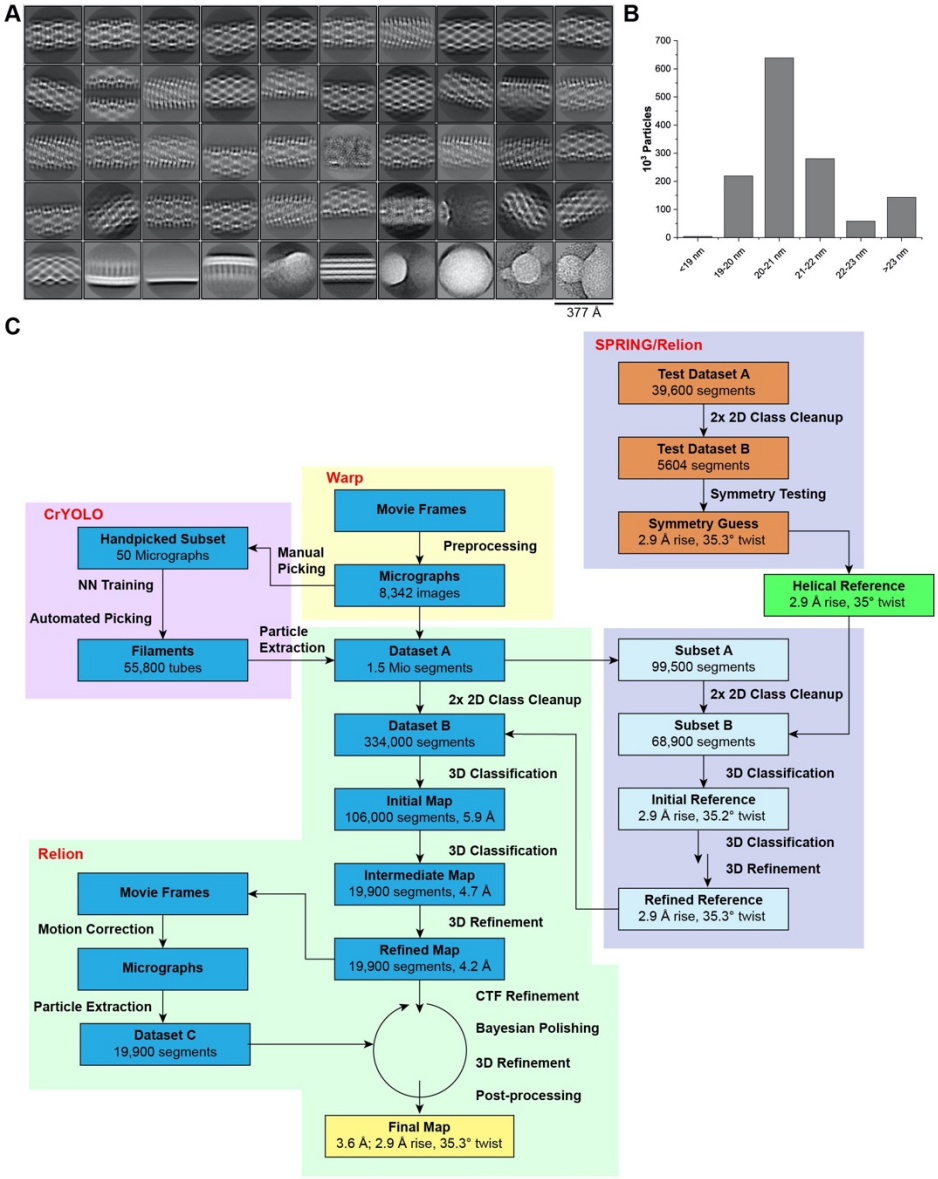

Figure S1. Cryo-EM sample characteristics of PspA and image processing workflow.

(A) Gallery of 2D class averages from initial 1.5 million segment data set. (B) Histogram showing distribution of measured widths of PspA rods. (C) Basic image processing workflow of PspA structure determination: PspA rods were segmented and a subset subjected to symmetry determination in SPRING followed by symmetry refinement in RELION. Once the symmetry was determined, RELION was used for final 3D structure determination of PspA including CTF refinement and Bayesian polishing.

Figure S2

A **α0:** ELFNRVGRVLKSQLTHWQQQQ

Hydrophobicty:	**0.313**
Hydrophobic moment:	**0.520**
Net charge:	**2**
Polar residues:	**66.67%**
Nonpolar residues:	**33.33%**

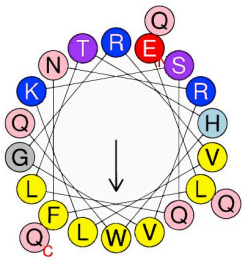

B **α5:** PLDKKFEQWEEWWAVEATLAAMKAR

Hydrophobicty:	**0.178**
Hydrophobic moment:	**0.180**
Net charge:	**-1**
Polar residues:	**52.00%**
Nonpolar residues:	**48.00%**

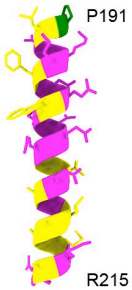

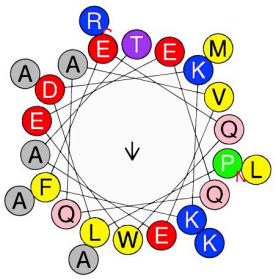

Figure S2. Helix wheel projections of (hypothetical) helix α0 and helix α5.

(A) Helix wheel projection of the hypothetical helix α0. (B) Helix wheel projection of helix α5. Projections were generated with HELIQUEST (Gautier et al., 2008).

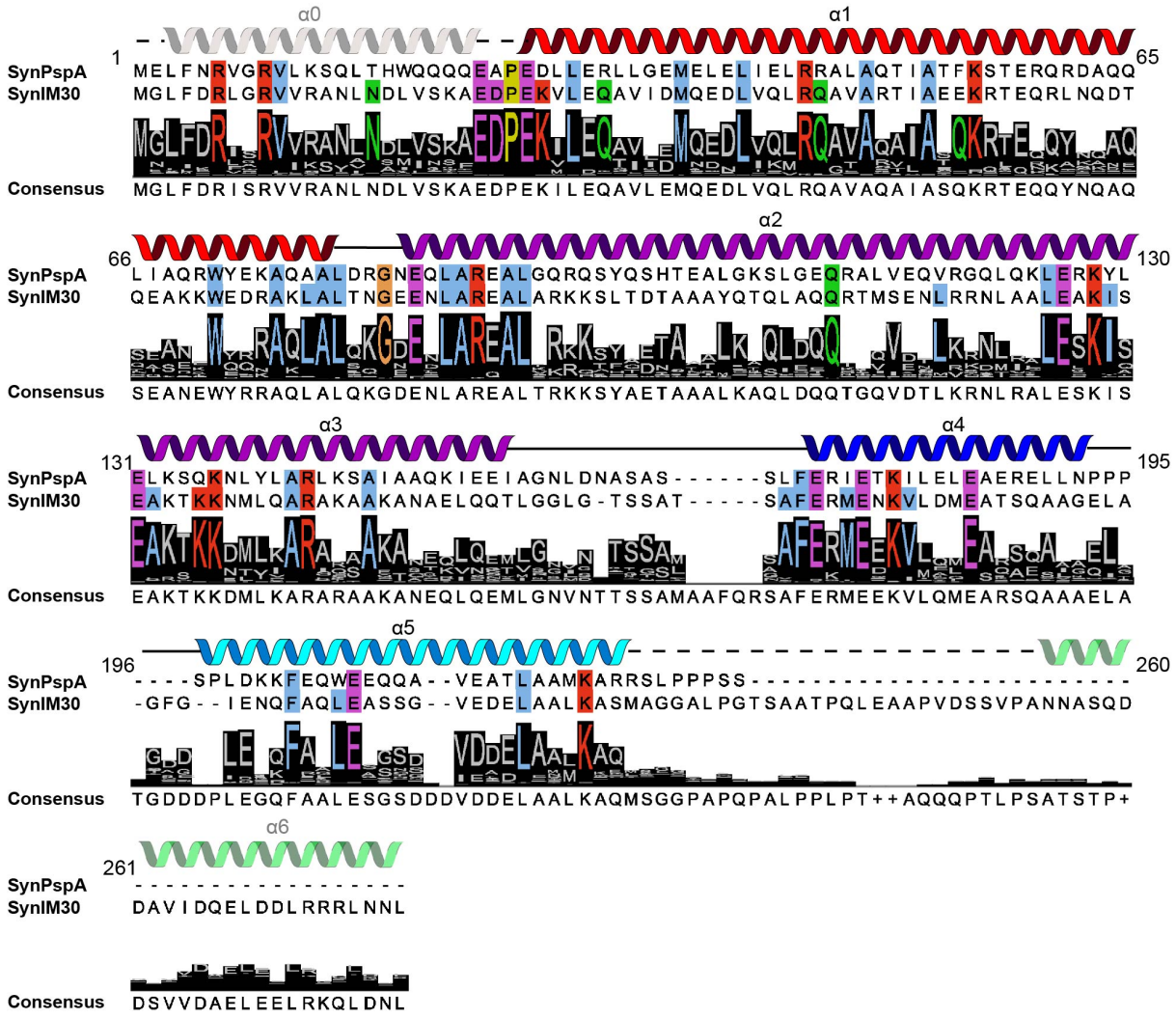

Figure S3. Sequence alignment of PspA/IM30 family proteins.

A conservation query for the PspA/IM30 protein was subjected to the ConSurf server (Ashkenazy et al., 2016) using the *Syn*PspA and the *Syn*IM30 sequence as input. The output of 250 sequences was aligned using ClustalW (Larkin et al., 2007) The resulting consensus sequence together with the *Syn*PspA and *Syn*IM30 were visualized in Jalview (Waterhouse et al., 2009) and superimposed with the PspA/IM30 secondary structure using the ESCRT-III helix nomenclature. Residues with >90% identity are colored by their properties according to the ClustalX coloring scheme.

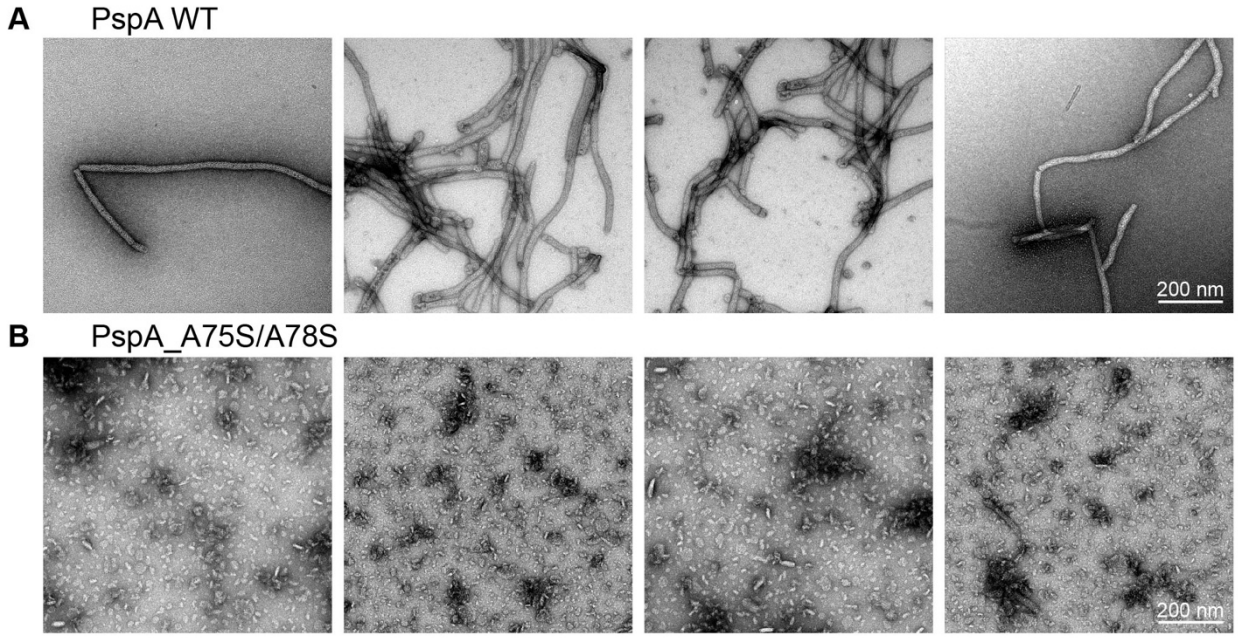

Figure S4. Negative-staining electron microscopy of PspA and PspA_A75S/A78S.

Micrographs of (A) PspA wildtype (WT) and (B) PspA_A75S/A78S negatively stained samples.

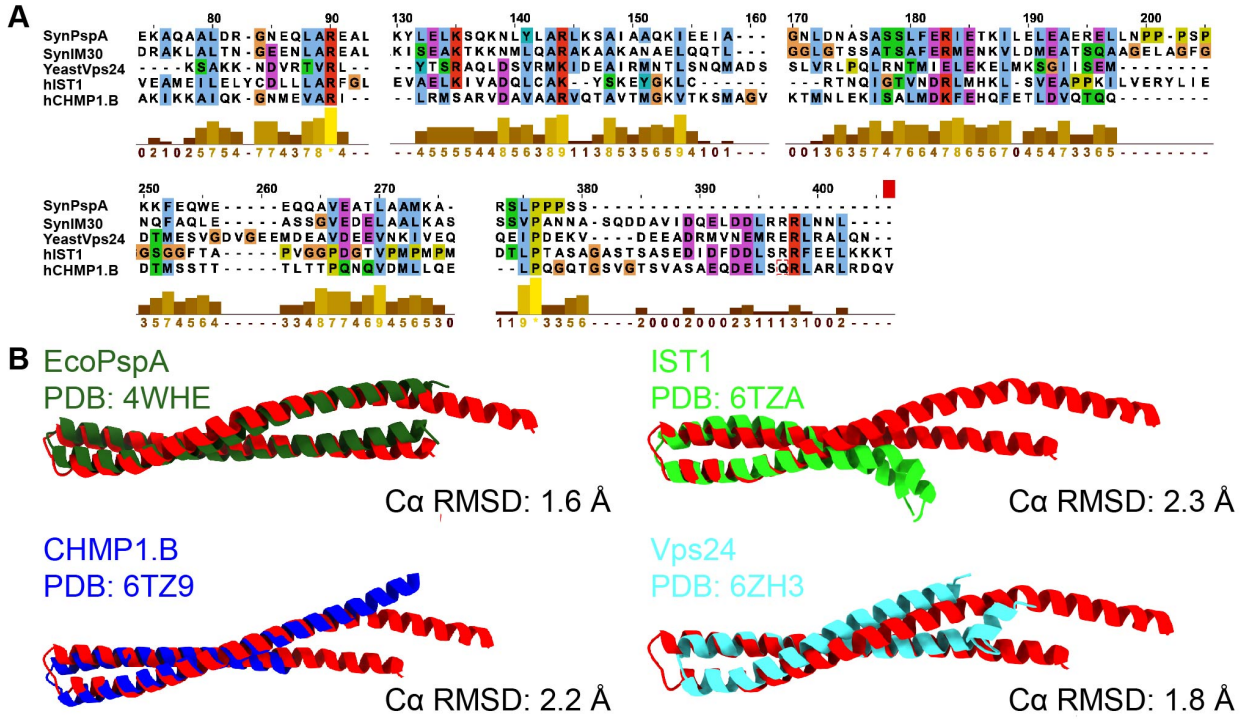

Figure S5. Comparison of α1/α2 hairpin motif of PspA with the eukaryotic ESCRT-III proteins IST1, CHMP1B and Vps24.

(A) Sequence alignment of PspA/IM30 with eukaryotic ESCRT-III proteins with bar graphs showing the alignment quality score as a measure of sequence similarity. Sequences were aligned using the T-Coffee webserver (Di Tommaso et al., 2011) and visualized with JalView (Waterhouse et al., 2009). (B) Structural superposition of the PspA hairpin with *Eco*PspA, IST1, CHMP1-B and Vps24. CA RMSD of residues approx. 50 – 90 (central hairpin) was calculated in Chimera using the "Match→Align" command.

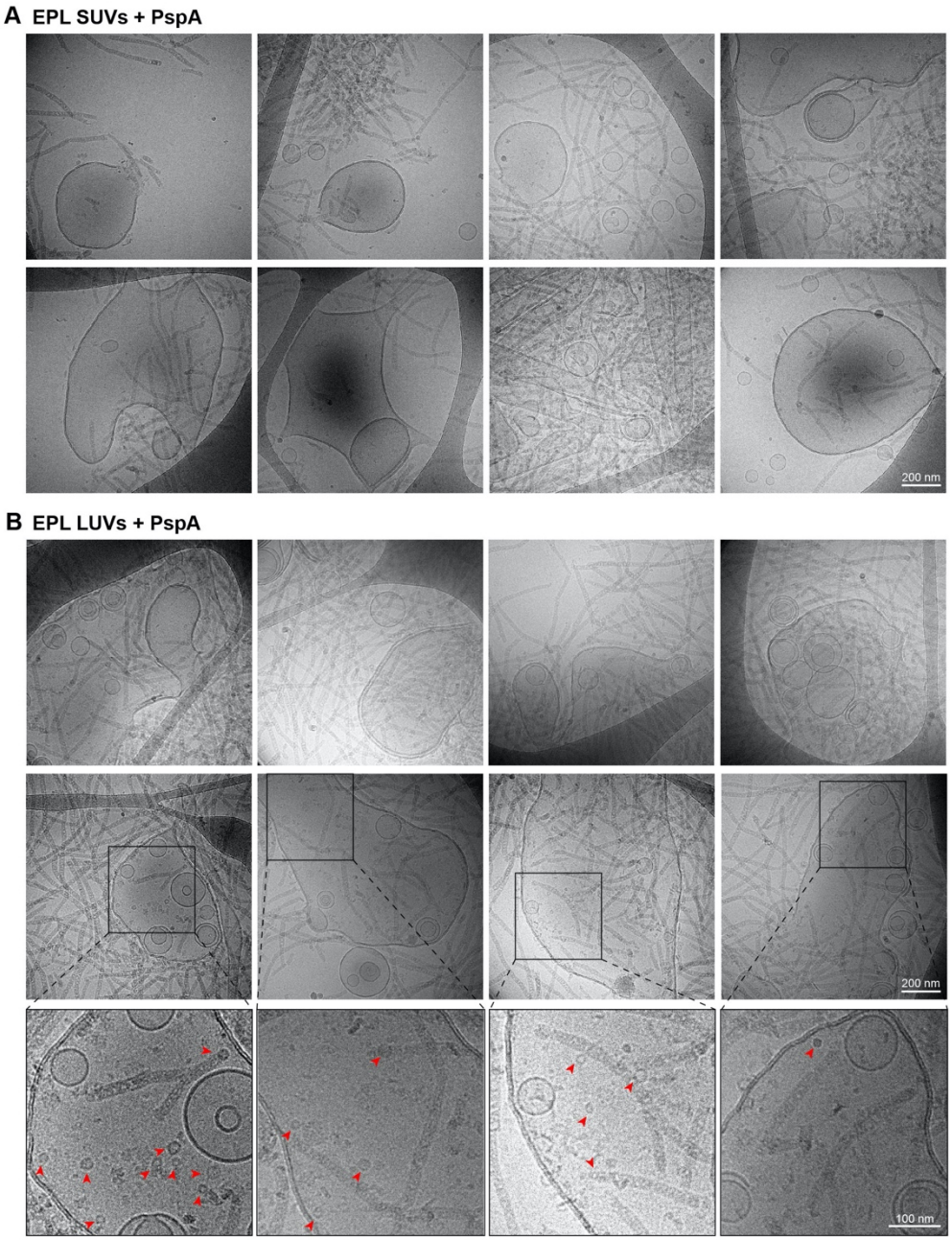

Figure S6. Gallery of *E. coli* polar lipid (EPL) vesicles after incubation with PspA rods.

(A) Electron cryo-micrographs of EPL small unilamellar vesicles (SUVs) in the presence of PspA rods. (B) Large unilamellar vesicles (LUVs) made from EPL in the presence of PspA rods. Bottom row shows magnified insets of the last row of LUV images. Red arrows indicate smaller oligomeric structures such as rings.

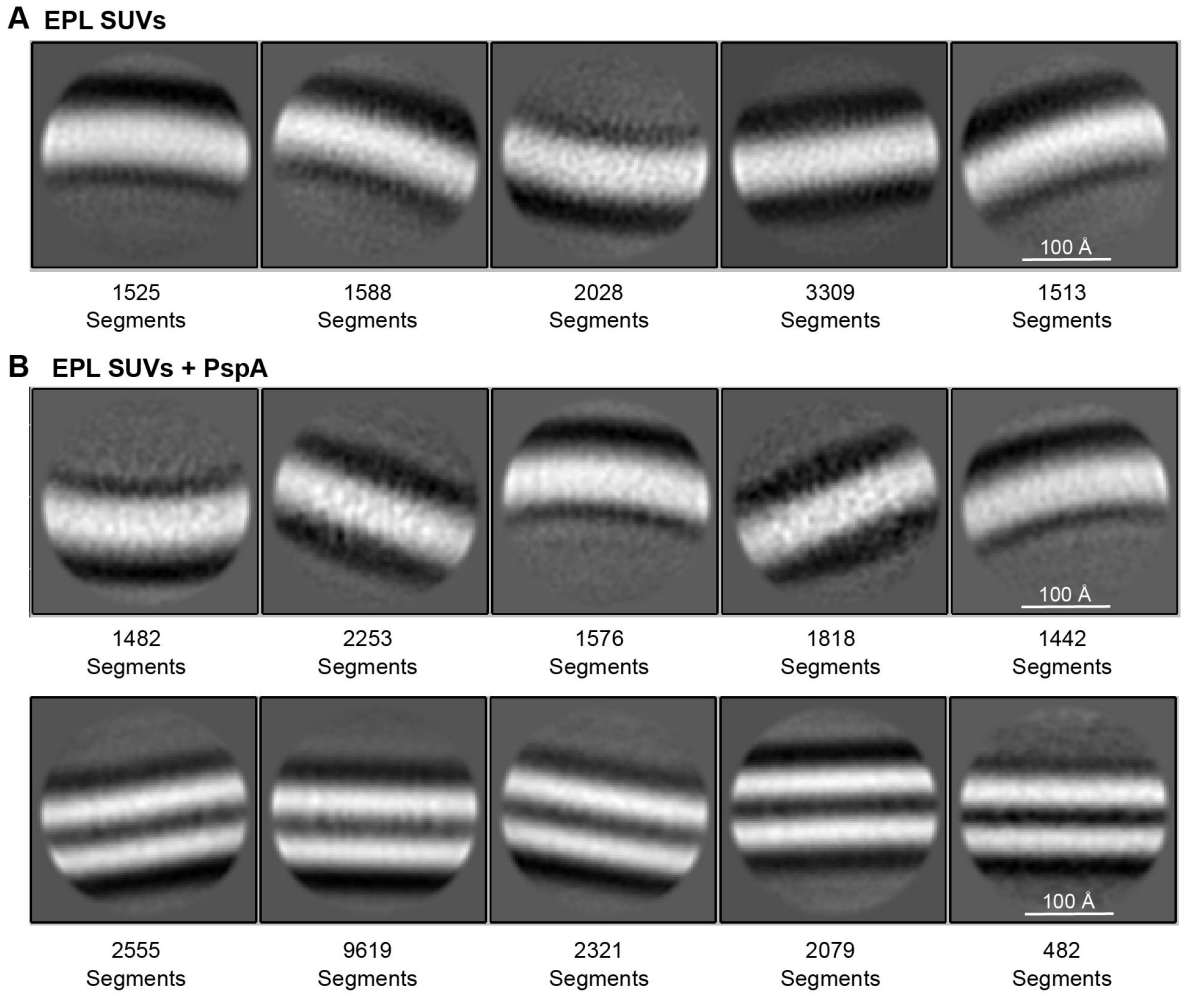

Figure S7. Class averages of segmented bilayers of small lamellar vesicles (SUVs) from *E. coli* polar lipids (EPL).

Class averages in the absence (A) and in the presence of PspA (B).

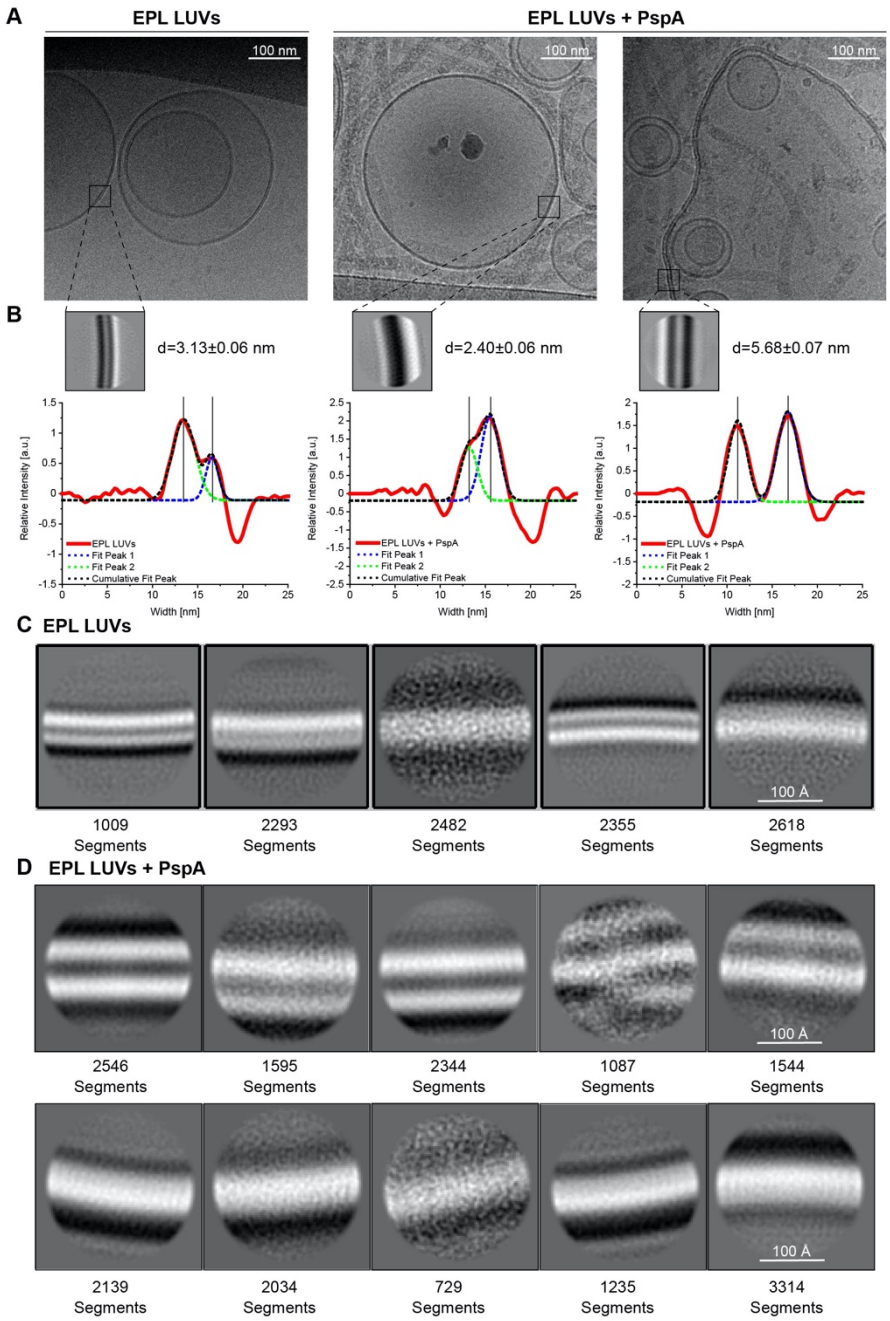

Figure S8. Cryo-EM image analysis of large lamellar vesicles (LUVs) from *E. coli* polar lipids (EPL) incubated with PspA rods.

(A) In the absence of PspA, EPL forms uniform round vesicles, whereas larger and deformed vesicles with a distinct bilayer leaflet separation in addition to a fraction of unaltered uniform vesicles were observed in presence of PspA. A gallery of EPL vesicles after incubation with PspA rods is shown in **Figure S6**. (B)

Detailed analysis of bilayer leaflet separation *d* in EPL vesicles determined from intensity profiles of class averages from segmented bilayers. Only class averages with clear features were used for the measurement. (n=3 class averages, errors represent SD). (C) Class averages in absence of PspA (D) Class averages in presence of PspA.